JOURNAL OF PETROLOGY | VOLUME 55 | NUMBER 12 | PAGES 2311–2346 | 2014 | doi:10.1093/petrology/egu058

Crystal Storage and Transfer in Basaltic Systems: the Skuggafjöll Eruption, Iceland

DAVID A. NEAVE[1]*, JOHN MACLENNAN[1], MARGARET E. HARTLEY[1], MARIE EDMONDS[1] AND THORVALDUR THORDARSON[2]

[1]DEPARTMENT OF EARTH SCIENCES, UNIVERSITY OF CAMBRIDGE, DOWNING STREET, CAMBRIDGE CB2 3EQ, UK

[2]FACULTY OF EARTH SCIENCES, UNIVERSITY OF ICELAND, ASKJA, STURLUGATA 7, 101 REYKJAVIK, ICELAND

RECEIVED JANUARY 20, 2014; ACCEPTED SEPTEMBER 26, 2014
ADVANCE ACCESS PUBLICATION OCTOBER 31, 2014

Magma mixing and crystal mush disaggregation are important processes in basaltic magma reservoirs. We carried out a detailed petrological and geochemical study on a highly plagioclase-phyric eruption within the Eastern Volcanic Zone of Iceland—the Skuggafjöll eruption—to investigate crystal storage and transport processes within a single magmatic system. Crystal content and phase proportions vary between samples: the least phyric samples have phase proportions similar to the low-pressure, three-phase gabbro eutectic (plg:cpx:ol ~ 11:6:3), whereas highly phyric samples are strongly enriched in plagioclase (plg:cpx:ol ~ 8:1:1). Statistically significant geochemical variability in 28 whole-rock samples collected across the eruption can be accounted for by variable accumulation of a troctolitic assemblage containing plagioclase and olivine in an approximately 9:1 ratio. Two macrocryst assemblages are defined using compositional and textural information recorded in QEMSCAN® images: a primitive assemblage of high-anorthite plagioclase ($An_{>83}$) and high-forsterite olivine ($Fo_{>84}$), and an evolved assemblage of low-anorthite plagioclase ($An_{<79}$), low-forsterite olivine ($Fo_{<82}$) and clinopyroxene (Mg# ~ 82). Plagioclase and olivine have strongly bimodal composition distributions whereas the composition distribution of clinopyroxene is unimodal. The mean trace element composition of melt inclusions hosted within high-forsterite olivine and high-anorthite plagioclase macrocrysts is the same (mean Ce/Y ~ 0·47–0·48), confirming that both primitive macrocryst phases crystallized from the same distribution of melts. Clinopyroxene macrocrysts and matrix glasses are in Ce/Yb equilibrium with each other, indicating that the evolved assemblage crystallized from melts with a more incompatible trace element-enriched composition (mean Ce/Y ~ 0·65–71) than the primitive assemblage. Variability in whole-rock, macrocryst and melt inclusion compositions suggests that the Skuggafjöll magma experienced two stages of crystallization. Primitive macrocrysts crystallized first from incompatible trace element-depleted melts within a shallow crustal magma reservoir. These primitive macrocrysts were subsequently stored in crystal mushes that ultimately disaggregated into an evolved and incompatible trace element-enriched magma from which the evolved assemblage crystallized. On average, ~17% of the erupted magma at Skuggafjöll is composed of accumulated macrocrysts entrained from crystal mushes. The timescale between mush disaggregation and eruption, during which crystal accumulation occurred, was short—of the order of years—according to simple diffusion calculations. Striking petrological similarities between Skuggafjöll and other highly phyric eruptions both in Iceland and along mid-ocean ridges indicate that crystal accumulation by mush disaggregation is likely to be an important mechanism for generating highly phyric magmas in basaltic plumbing systems.

KEY WORDS: *mush disaggregation; magma reservoir; Iceland; plagioclase; basalt*

INTRODUCTION

Highly phyric basalts and crystal mush disaggregation

Crystal contents of mid-ocean ridge basalts (MORBs) vary greatly (e.g. Bryan & Moore, 1977; Bryan, 1983). Plagioclase ultraphyric basalts (PUBs), which erupt on-axis in regions of ultraslow to moderate spreading, off-axis along all ridges and at ocean islands, represent some of the most crystal-rich magmas erupted at the Earth's surface (Flower, 1980; Bryan *et al.*, 1981; Cullen *et al.*, 1989; Hansen & Grönvold, 2000; Hellevang & Pedersen, 2008;

*Corresponding author. Telephone: +44 (0)1223 333400. Fax: 01223 333450. E-mail: dan27@cam.ac.uk

Lange *et al.*, 2013*a*). These highly phyric lavas are characterized by high crystal contents (>10 vol. %, but often 30 vol. %) and plagioclase-to-olivine ratios in excess of the approximately 7:3 ratio expected during cotectic crystallization of primitive basalts at low pressure (Bryan, 1983; Hellevang & Pedersen, 2008; Lange *et al.*, 2013*a*). Plagioclase macrocrysts in PUBs are often too anorthitic to be in equilibrium with the melts in which they are carried (Dungan & Rhodes, 1978; Cullen *et al.*, 1989; Hansen & Grönvold, 2000). The composition of melt inclusions hosted within anorthitic plagioclase macrocrysts from highly phyric basalts further reinforces their primitive character (Sinton *et al.*, 1993; Adams *et al.*, 2011). Multistage magmatic evolution histories are thus often required to explain the formation of highly phyric basalts (e.g. Dungan & Rhodes, 1978; Cullen *et al.*, 1989; Lange *et al.*, 2013*a*).

Plagioclase flotation has been proposed as a mechanism for generating high crystal contents and high plagioclase proportions in PUBs (e.g. Flower, 1980; Cullen *et al.*, 1989; Hellevang & Pedersen, 2008). Recently, Lange *et al.* (2013*a*) reassessed whether anorthitic plagioclase is able to float in primitive basalts, arguing instead that high modal abundances of plagioclase are generated by magmas interacting with primitive cumulates formed during earlier phases of crystallization. Plagioclase macrocrysts from PUBs are more anorthitic (An_{85-90}; Lange *et al.*, 2013*a*) than plagioclase macrocrysts in anorthosites from layered intrusions that are thought to form by flotation (e.g. An_{60-68} in anorthosites from the Sept-Îles layered intrusion; Namur *et al.*, 2011*a*) and are thus more likely to sink by virtue of their higher density. Sr isotopic disequilibrium between high-anorthite plagioclase macrocrysts and their carrier melts further supports models of highly phyric basalt genesis by crystal mush disaggregation where primitive crystals grow from earlier and geochemically distinct batches of melt (Halldorsson *et al.*, 2008; Lange *et al.*, 2013*b*).

Crystal mush disaggregation can be identified in lavas from the compositional variability in whole-rock samples (Salaün *et al.*, 2010; Passmore *et al.*, 2012), as well as from the composition and texture of the macrocrysts and nodules they contain (Hansen & Grönvold, 2000; Gurenko & Sobolev, 2006; Ridley *et al.*, 2006; Holness *et al.*, 2007, 2013; Costa *et al.*, 2010). Understanding mush disaggregation in basaltic magma reservoirs is important for a number of reasons: (1) short timescales between disaggregation and eruption (e.g. Costa *et al.*, 2010) suggest that eruption triggering and mush disaggregation may be closely linked; (2) mush crystals contain important information about the depths and conditions of magma storage; (3) disaggregated crystals and nodules provide a key link between volcanic and plutonic processes, and can be used to place constraints on the structure and mineralogy of the crust.

PUBs are common across Iceland (Jakobsson, 1979), but are best documented in the Eastern Volcanic Zone (EVZ) (Hansen & Grönvold, 2000; Halldorsson *et al.*, 2008), Iceland's most volcanically productive neovolcanic rift zone (Thordarson & Höskuldsson, 2008). Iceland provides an ideal location for studying basaltic magmatism because of the ease of access to whole flow fields. Although a number of studies have investigated the causes of geochemical variation within single Icelandic eruptions (Sigmarsson *et al.*, 1991; Maclennan *et al.*, 2003*b*; Halldorsson *et al.*, 2008; Eason & Sinton, 2009; Passmore *et al.*, 2012), only the study of Halldorsson *et al.* (2008) has focused on a highly plagioclase-phyric basalt, the voluminous (>25 km^3) Thjórsá lava.

The aim of the present study was to investigate the causes of geochemical variability within the highly phyric Skuggafjöll eruption from the EVZ. Lavas from the Skuggafjöll eruption contain large volumes of glassy to microcrystalline groundmass and are thus well suited for combined microanalytical and textural study. Textural associations between macrocrysts and their constituent zones are preserved in the Skuggafjöll eruption, in contrast to the crystalline Thjórsá lava, from which Halldorsson *et al.* (2008) were restricted to analysing mechanically separated macrocryst and groundmass fragments. However, at Skuggafjöll, eruption age and volume are poorly constrained.

Geochemical variability has been investigated at a range of scales in the Skuggafjöll eruption: between whole-rock samples collected across the edifice, between macrocrysts within whole-rock samples and between melt inclusions hosted within these macrocrysts. Relationships between different components of the erupted magma were assessed using a range of petrographic, geochemical, microanalytical and textural techniques, including QEMSCAN® imaging that combines spatial and compositional information about rock microstructure on the thin-section scale. The primary finding is that the whole-rock compositional variability in the Skuggafjöll eruption is controlled by variable accumulation of a troctolitic assemblage containing primitive macrocrysts. The accumulated assemblage contains high-anorthite plagioclase and high-forsterite olivine macrocrysts that are far from being in equilibrium with the carrier melt and are present in strongly non-cotectic proportions. An evolved, gabbroic assemblage that contains lower anorthite plagioclase, lower forsterite olivine and clinopyroxene, which crystallized from the carrier liquid following mush disaggregation, occurs alongside the primitive assemblage. Through gaining an improved understanding of mush disaggregation and entrainment—two processes that are intimately linked with magma recharge and eruption—it is possible to place firmer constraints on magma reservoir processes that lead to the generation of highly phyric basalts in Iceland and beyond.

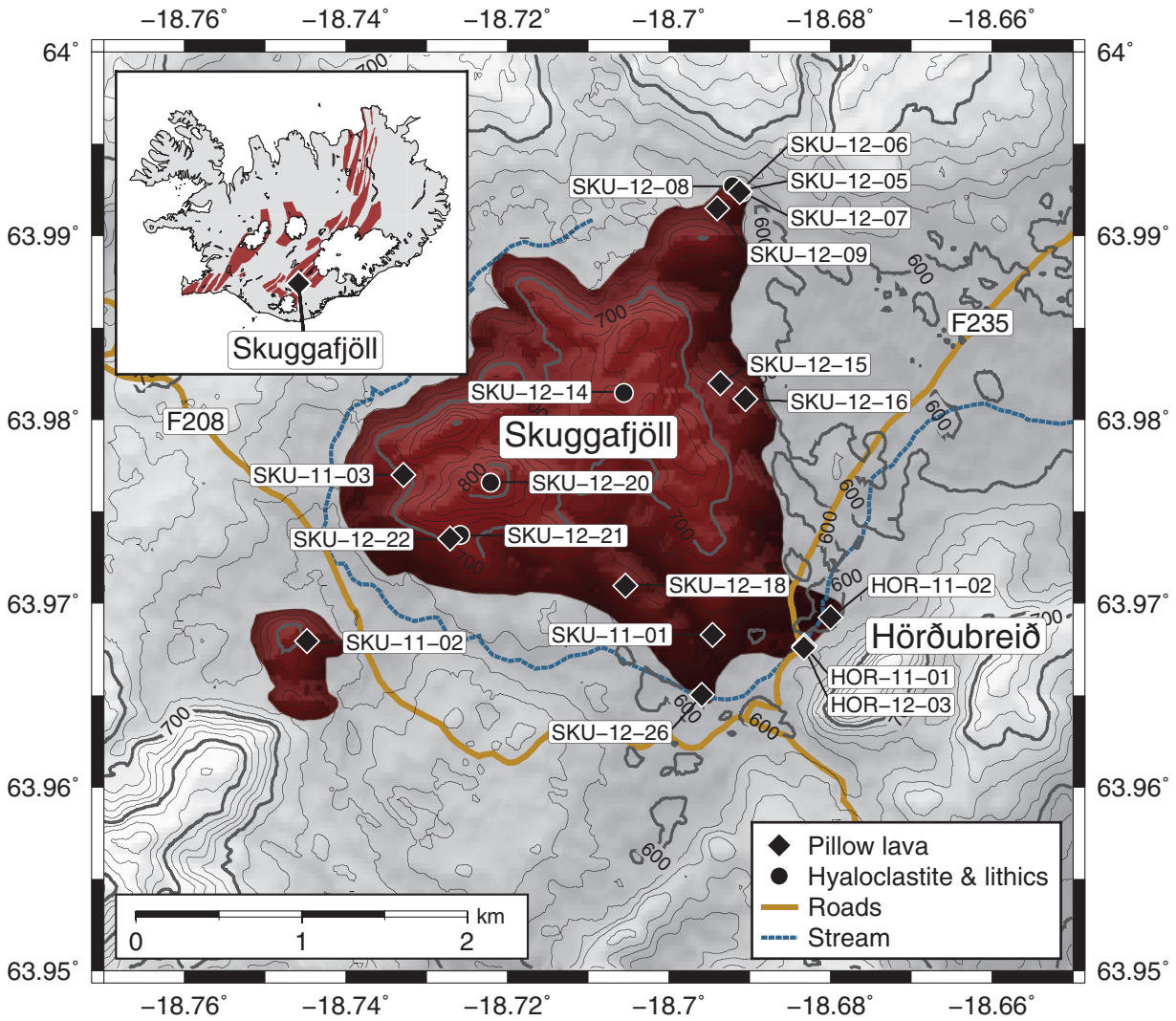

Fig. 1. Map showing the location of samples used in the study. The inset map shows the location of Skuggafjöll in the EVZ of Iceland. The approximate extent of lava and hyaloclastite associated with the Skuggafjöll eruption is shown by the area of darker shading. The NW flank of Hörðubreið forms part of the Skuggafjöll eruptive unit. Sampling locations for both pillow lavas and hyaloclastite, along with sample numbers, are shown on the map by diamonds and circles respectively. Basaltic lithic samples were also collected from within the hyaloclastite. Pillow lavas are restricted to the lower flanks of the mountain, with the higher slopes being composed of hyaloclastite. No subaerial lavas were found at the top of the mountain.

The Skuggafjöll eruption

Skuggafjöll is an 820 m high mountain that forms part of a NE–SW-striking hyaloclastite ridge (or tindar) approximately halfway between the Mýrdalsjökull and Vatnajökull glaciers in southern Iceland (Fig. 1; 63·968°N, 18·695°W). The lower slopes of the mountain are composed of pillow lavas that are occasionally intercalated with hyaloclastite. Pillow lavas are highly, but variably, phyric, with >1 mm macrocrysts of plagioclase, olivine and clinopyroxene identifiable in the field. A transition from pillow lavas to hyaloclastite occurs halfway up the mountain at ~700 m elevation. The presence of pillow lavas and hyaloclastite indicates that Skuggafjöll formed when the EVZ was buried under ice, most probably during the last glaciation, thus giving a minimum eruption age of ~10 ka (Jakobsson & Gudmundsson, 2008). A minimum erupted volume of ~0·2 km^3 is estimated by approximating the shape of the edifice to a cone with a basal radius of 1 km and a height of 0·2 km. After accounting for erosion and burial by subsequent eruptions, the original erupted volume may have been substantially larger.

Matrix glasses and olivine-hosted melt inclusions from the Skuggafjöll eruption have been studied by Neave *et al.* (2014), and are amongst the most primitive compositions known from the EVZ. The trace element content of olivine-hosted melt inclusions from Skuggafjöll can be

accounted for by a combination of melt mixing and fractional crystallization (Neave *et al.*, 2014). Combined CO_2 and trace element systematics from the same inclusions are best explained by concurrent CO_2 exsolution, mixing and entrapment of melt. Melt inclusion data from Neave *et al.* (2014) are discussed further in subsequent sections alongside new plagioclase-hosted melt inclusion data.

Some notes on crystal terminology

Using genetic terms such as phenocryst or xenocryst to describe crystals in volcanic rocks has significant limitations (Davidson *et al.*, 2007; Ruprecht *et al.*, 2012; Thomson & Maclennan, 2013). Observations of isotopic disequilibrium between crystals and their carrier liquids led Davidson *et al.* (2007) to suggest that crystals out of equilibrium with their surroundings, but nevertheless sourced from the same magmatic system, could be referred to as antecrysts (after W. Hildreth at the 'Longevity and Dynamics of Rhyolitic Magma Systems' Penrose Conference, 2001). However, the limits of a magmatic system are difficult to define, especially in Iceland where mantle melting has been generating oceanic crust of similar composition at the same location for millions of years (Thomson & Maclennan, 2013). The non-genetic term macrocryst is thus used throughout to refer to crystals with a minimum long axis length of 150 μm. This definition is based on the minimum size of crystals in rapidly quenched, glassy portions of thin sections.

SAMPLE COLLECTION

Samples were collected during two field seasons in 2011 and 2012 and consist of 24 glassy to microcrystalline pillow lava hand specimens, two hyaloclastite hand specimens and three hyaloclastite-hosted basaltic lithic hand specimens. Many hyaloclastite-hosted lithic samples have glassy margins, and probably represent the remains of pillow lavas fragmented during phreatomagmatic activity. Weathered lavas containing yellow olivine, brown plagioclase or mud-filled vesicles were avoided during sampling. Particular attention was paid to collect samples with a wide range of macrocryst contents. Samples were collected only from flow lobes that were uniformly macrocryst-rich or macrocryst-poor to mitigate the effects of within-flow crystal sorting (e.g. Mathews *et al.*, 1964). The latitude, longitude and elevation of each sample were recorded using a hand-held global positioning system (GPS) with an accuracy of ~5 m. Sample locations are shown in Fig. 1 and are provided in Supplementary Data Electronic Appendix 1 (supplementary data are available for downloading at http://www.petrology.oxfordjournals.org).

PETROGRAPHY

Mineralogy

All samples are olivine, clinopyroxene and plagioclase phyric (Fig. 2). Spinel grains (chromites) are present as inclusions within plagioclase and olivine macrocrysts. Fe–Ti oxides are present only as small dendritic grains in the groundmass of the most crystalline samples, and are never observed in the glassy portions of thin sections.

Olivine macrocrysts are generally equant, subhedral and 150–1500 μm in size. Rare olivine grains up to 4 mm in size are present and are usually associated with large plagioclase macrocrysts. Spheroidal, glassy to cryptocrystalline melt inclusions up to ~300 μm in size occur in olivine macrocrysts. Clinopyroxene macrocrysts are generally equant to prismatic and 150–2250 μm in size. Both hourglass and complex sector zoning are visible in some clinopyroxene grains under crossed polars. Concentric zoning is also visible in clinopyroxene macrocrysts with and without sector zoning. Plagioclase macrocrysts are generally 150–5000 μm in size, but may be up to 12 mm. Large plagioclase grains (generally >600 μm) have low aspect ratios (length/width ~1·5, up to a maximum of ~2) and stubby tabular to prismatic habits, whereas small grains (<600 μm) have higher aspect ratios (length/width >2, up to a maximum of ~5) and elongate tabular habits. When discussing plagioclase macrocrysts, 'large' and 'small' may be considered synonymous with 'low aspect ratio' and 'high aspect ratio'. Discrete cores and rims are visible under crossed polars in large plagioclase macrocrysts. Large plagioclase macrocrysts also exhibit a wide range of textures: some contain no melt inclusions, whereas others contain large numbers of small (<10 μm) melt inclusions both in the centre of crystal cores and in concentric bands parallel to crystal faces. Rare plagioclase grains show striking sieve textures. Occasional glassy to cryptocrystalline melt inclusions up to ~150 μm in size are present within plagioclase macrocrysts.

Macrocrysts of all phases occur as single grains and within monomineralic and polymineralic glomerocrysts. Glomerocrysts can be categorized into two groups: large and small. Large glomerocrysts (>2 mm; Fig. 2a), which contain large, low aspect ratio plagioclase grains (>1 mm), are associated with large olivine grains (>500 μm). Clinopyroxene occurs only as small grains around the edge of large glomerocrysts. Plagioclase grains are often oriented at high angles to each other (Fig. 2b). Single glomerocrysts also contain plagioclase macrocrysts with different textures and melt inclusion contents. Small glomerocrysts (<2 mm), which contain clinopyroxene and plagioclase grains in ophitic arrangement, are generally smaller than ~1 mm (Fig. 2c). Small olivine grains (<500 μm) may also be present in variable proportions within small glomerocrysts.

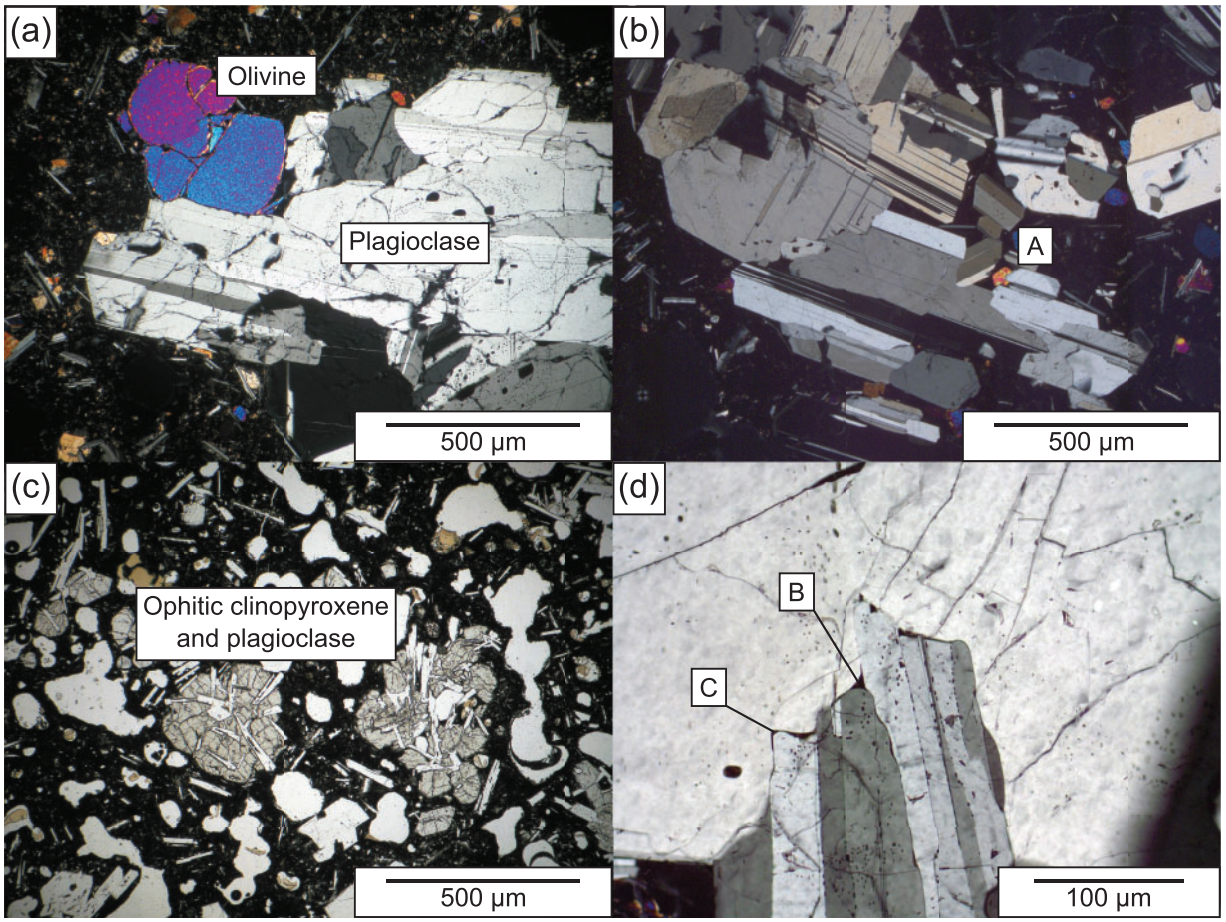

Fig. 2. Textures observed in typical pillow lava samples from Skuggafjöll. (a) Photomicrograph (crossed polars) of sample SKU-11-01A, showing part of a glomerocryst containing large macrocrysts of plagioclase and olivine set in a fine-grained groundmass of plagioclase, olivine and clinopyroxene. Both large olivine and large plagioclase grains occur as single macrocrysts, as well as in monomineralic and polymineralic glomerocrysts. (b) Photomicrograph (crossed polars) of sample HOR-12-03A showing a plagioclase-dominated glomerocryst. The numerous intergrown plagioclase grains resting at high angles to each other (marked 'A') should be noted. (c) Photomicrograph (plane polars) of sample SKU-11-02A. Two glomerocrysts containing high-relief clinopyroxene and low-relief plagioclase in ophitic arrangement are visible in the centre of the image. The glomerocrysts are set in a dark and vesicular mesostasis. (d) Photomicrograph (crossed polars) of sample HOR-11-02B. The presence of melt pores at plg–plg–plg boundaries (marked 'B') and thin melt films between intergrown plagioclase grains (marked 'C') should be noted.

Point counting

The macrocryst phase proportions and vesicularity of pillow lava and basaltic lithic samples were determined using point counting. A mechanical slide holder was moved in steps of 0·3 mm in both the x and y directions, generating between 1500 and 2000 points per thin section depending on the sample size. Olivine, clinopyroxene and plagioclase, groundmass and vesicles were counted as separate phases. Crystals with long axes under the size threshold of 150 μm were counted as groundmass.

Vesicle-free macrocryst mass fractions were calculated from point counting data using the following phase densities: 3·3 g cm^{-3} for olivine, 3·2 g cm^{-3} for clinopyroxene, 2·7 g cm^{-3} for plagioclase and 2·7 g cm^{-3} for the groundmass. Both raw point counting data and macrocryst mass fractions are reported in Table 1. The mean macrocryst mass fraction of measured samples is 30·4 ± 10·7% (1σ) with a range from 5·9 to 46·9%. The mean proportions of macrocryst phases are plg:cpx:ol in the ratio 74:17:9 (Fig. 3). However, phase proportions vary substantially between samples. Poorly phyric samples (macrocryst mass fraction <20%) have phase proportions similar to those expected during low-pressure crystallization at the three-phase gabbro eutectic (plg:cpx:ol in the approximate ratio 11:6:3; Yang *et al.*, 1996). Highly phyric samples (macrocryst mass fractions >35%) contain plagioclase proportions of up to 90% (Fig. 3; Table 1), which is much higher than expected during anhydrous crystallization along either the gabbroic or the ol–plg cotectic (Grove *et al.*, 1992; Yang *et al.*, 1996).

Table 1: Raw point counting data and macrocryst mass fractions for pillow basalt and basaltic lithic samples from Skuggafjöll

Sample	Raw counts					Mass fractions (%)			
	plg	cpx	ol	gm	ves	plg	cpx	ol	macro
HOR-11-01A	489	54	32	773	512	35·8	4·7	2·9	43·4
HOR-11-01B	543	72	39	1028	394	31·8	5·3	2·8	39·9
HOR-11-01C	381	63	32	911	290	27·0	5·3	2·8	35·2
HOR-11-02A	453	107	33	716	372	33·6	9·2	3·1	45·9
HOR-11-02B	429	112	41	950	275	27·4	8·5	3·2	39·1
SKU-11-01A	780	63	47	1029	360	39·9	3·9	2·9	46·8
SKU-11-01B	158	65	22	1183	261	11·0	5·3	1·8	18·1
SKU-11-02A	364	94	30	1229	492	20·9	6·4	2·1	29·4
SKU-11-02B	505	104	34	978	483	30·6	7·5	2·5	40·6
SKU-12-06A	149	31	15	926	540	13·2	3·3	1·6	18·1
SKU-12-06B	542	31	24	967	268	34·4	2·3	1·9	38·6
SKU-12-07	326	22	40	914	444	24·8	2·0	3·7	30·5
SKU-12-09A	40	18	12	1222	312	3·1	1·6	1·1	5·9
SKU-12-09B	80	35	16	861	332	8·0	4·1	2·0	14·1
SKU-12-09C	496	45	39	957	247	31·9	3·4	3·1	38·4
SKU-12-14A	402	25	42	1078	268	25·8	1·9	3·3	30·9
SKU-12-14B	299	38	24	961	223	22·4	3·4	2·2	28·0
SKU-12-15A	63	48	12	719	684	7·4	6·7	1·7	15·8
SKU-12-15B	207	20	23	624	527	23·4	2·7	3·2	29·3
SKU-12-15C	216	29	14	829	246	19·7	3·1	1·6	24·4
SKU-12-16	101	44	23	1092	429	7·9	4·1	2·2	14·2
SKU-12-18	323	56	41	931	140	23·6	4·8	3·7	32·1
SKU-12-21	289	42	14	714	291	27·0	4·7	1·6	33·3
SKU-12-22	489	80	22	967	342	31·0	6·0	1·7	38·7
SKU-12-26	307	29	33	789	273	26·2	2·9	3·4	32·6
HOR-12-03A	347	41	25	883	303	26·5	3·7	2·3	32·6
HOR-12-03B	156	58	23	864	350	14·0	6·2	2·5	22·6

plg, plagioclase; cpx, clinopyroxene; ol, olivine; gm, groundmass; ves, vesicles; macro, macrocrysts.

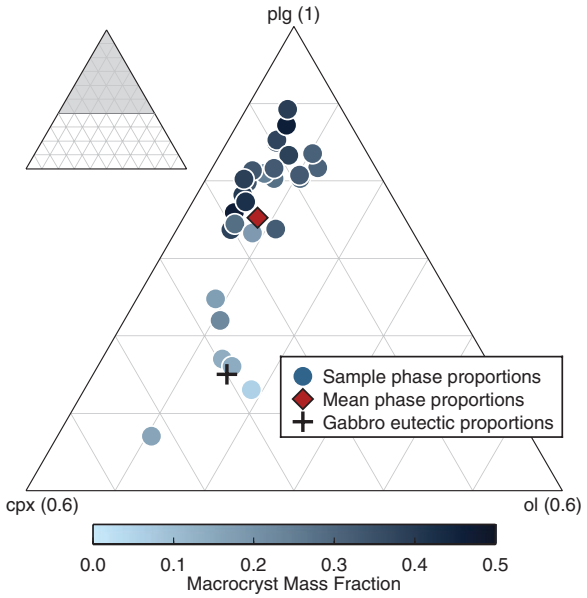

Fig. 3. Ternary plot showing the relative mass proportions of plagioclase, clinopyroxene and olivine in pillow basalt and basaltic lithic samples from Skuggafjöll, as determined by point counting. Point counting data points are coloured based on the mass fraction of all macrocrysts. Mean phase proportions of all samples and typical low-pressure gabbro eutectic proportions from Yang *et al.* (1996) are indicated

The precision of phase proportion measurements was estimated by repeat counting of eight samples, providing a total of 24 repeats. Each thin section was assumed to be representative of the whole sample and crystals were assumed to be randomly oriented throughout. The 1σ relative precision of counts is estimated as 4·5% for plagioclase, 17·7% for clinopyroxene, 23·0% for olivine and 5·0% for the total macrocryst content.

Crystal size distributions

Crystal size distributions (CSDs) contain information about the nucleation and growth of crystals in magma (e.g. Cashman & Marsh, 1988; Marsh, 1988). CSDs are also highly sensitive to mixing crystal populations of different sizes and ages (Marsh, 1998). Populations of larger, hence older, crystals show shallower negative gradients on plots of crystal length against the natural logarithm of population density than populations of smaller, hence younger, crystals (e.g. Higgins, 1996).

Plagioclase, clinopyroxene and olivine CSDs were calculated for Skuggafjöll by digitally tracing macrocrysts and vesicles on high-resolution (4000 dpi) scans of three thin sections. Macrocrysts were defined as having a long axis length of >150 μm, consistent with the size threshold used in point counting. Thin sections were chosen to represent a wide range of macrocryst contents: HOR-11-01B has a macrocryst content of 39·9%, SKU-11-02A has a macrocryst content of 29·4%, and SKU-11-01B has a macrocryst content of 18·1% (Table 1). Macrocryst and vesicle size data were extracted from images, to which thresholds had been applied, using the 'analyse particles' tool in ImageJ. CSD were calculated over areas of ~700 mm^3, using 1751–3529 crystals for plagioclase, 214–442 crystals for clinopyroxene and 110–396 crystals for olivine (Fig. 4).

The habit of plagioclase macrocrysts in Skuggafjöll varies significantly with crystal size: large grains have stubby, low aspect ratio habits (length/width ~1·5); and small grains have elongate, high aspect ratio habits (length/width >2) (Fig. 4d–f). A change in crystal habit occurs at a crystal length of ~600 μm, but is not clearly

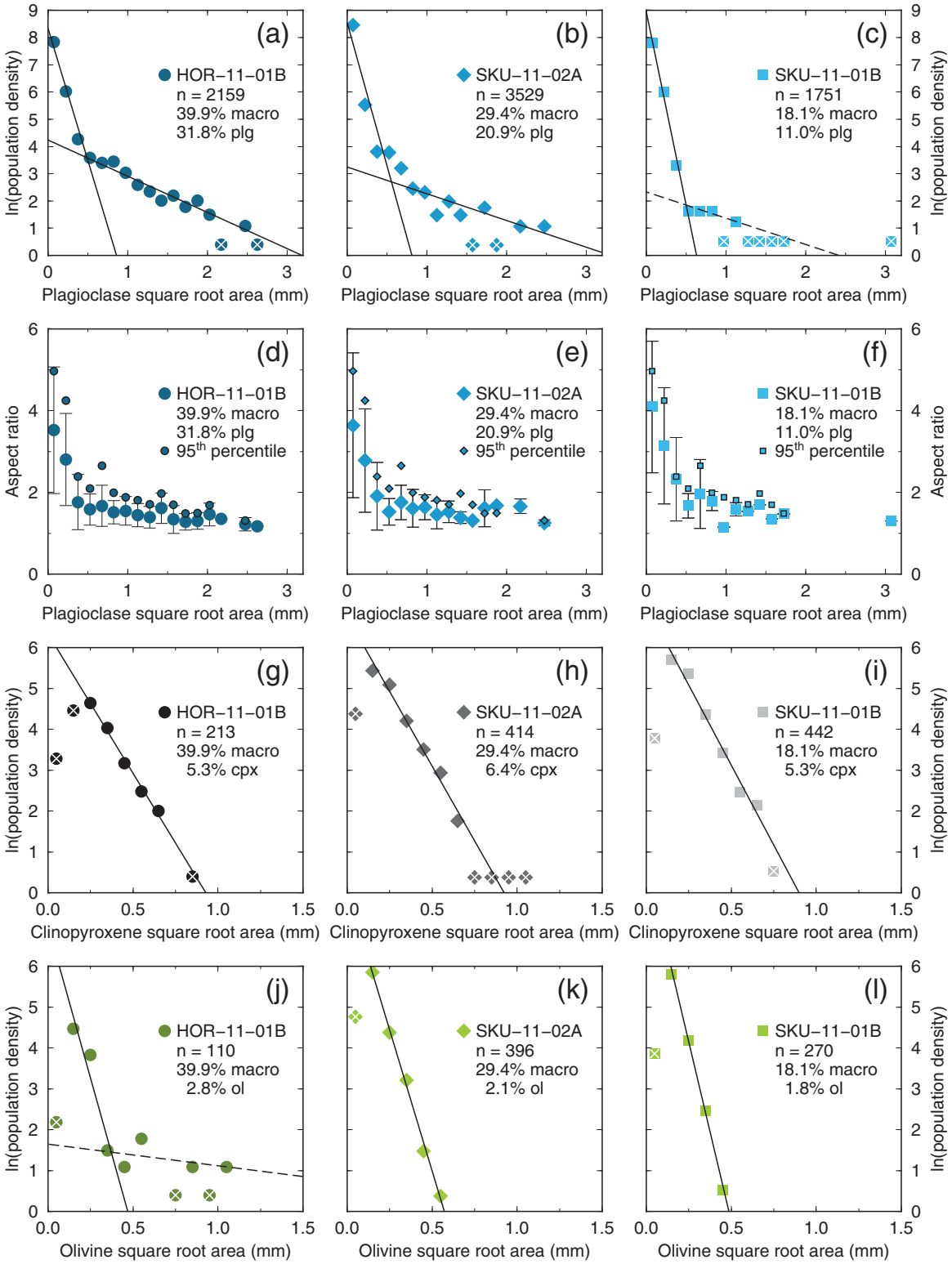

Fig. 4. Crystal size distributions (CSDs) for plagioclase (a–c), clinopyroxene (g–i) and olivine (j–l) in three samples with variable crystal contents: HOR-11-01B, 39·9% macrocryst mass fraction; SKU-11-02A, 29·4% macrocryst mass fraction; SKU-11-01B, 18·1% macrocryst mass fraction. Data are plotted as the square root of crystal area versus population density. Linear regressions through coherent macrocryst populations are shown as continuous black lines. Poorly constrained regressions through possible macrocryst populations are shown as a dashed black line. Data excluded from regressions are shown with white crosses. Data were excluded from regressions when size bins contain only a single crystal or when crystals were too small to be resolved. Plagioclase macrocrysts are grouped into 150 μm bins, whereas clinopyroxene and olivine macrocrysts are grouped into 100 μm bins. Mean plagioclase aspect ratios for each size bin with 1σ error bars are shown in (d)–(f). Where bins contain sufficient crystals, 95th percentiles, which give a robust estimate of maximum aspect ratio, are shown with black rimmed symbols. (d–f) Plots of aspect ratio versus square root of crystal area for plagioclase.

defined: some low aspect ratio plagioclase macrocrysts are shorter than 600 μm and some high aspect ratio plagioclase macrocrysts are longer than 600 μm. To account for this variability in crystal habits, CSDs were calculated using the square root of macrocryst areas instead of macrocryst lengths. Using this method, elongate crystals with small areas for a given crystal length can be distinguished from stubby crystals with larger areas for the same crystal length. No stereological conversions were applied. CSDs were calculated using linearly spaced 150 μm bins for plagioclase and linearly spaced 100 μm bins for clinopyroxene and olivine. Although the square root of macrocryst area is a more abstract dimension than macrocryst length, it is thus possible to avoid introducing new errors from applying stereological corrections that are inappropriate across the whole CSD. Macrocryst areas are provided in Supplementary Data Electronic Appendix 2.

Plagioclase CSDs are determined accurately because of the large number of crystals used (1751–3529; Fig. 4a–c). All three plagioclase CSDs have pronounced kinks at ~600 μm square root area, separating shallow gradients at large crystal sizes from steep gradients at small crystal sizes. Such kinked CSD are best modelled as a mixture of two crystal populations, one with a small crystal size and one with a large crystal size (e.g. Higgins, 1996). Regressions through the different populations give characteristic crystal lengths (L_D) of 70–100 μm for the population of small macrocrysts and 700–1030 μm for the population of large macrocrysts (where $L_D = -1/\text{slope}$; Higgins & Chandrasekharam, 2007). It should be noted that L_D is the square root of macrocryst area when using the square root of crystal area as a measure of crystal size. Regression lines drawn through coherent plagioclase populations indicate that, whereas populations of small, high aspect ratio macrocrysts in all three thin sections are similar (i.e. have similar slopes and intercepts in log–linear space), populations of large, low aspect ratio macrocrysts are different (i.e. have different intercepts in log–linear space).

Clinopyroxene CSDs are determined moderately well, with between 214 and 442 crystals used in calculations (Fig. 4g–i). In contrast to plagioclase CSDs, clinopyroxene CSDs are linear and exhibit no consistent changes in gradient. Assuming that nucleation and growth rates are constant, linear CSDs suggest that there is a single population of clinopyroxene present at Skuggafjöll.

Olivine CSDs are more ambiguous than plagioclase and clinopyroxene CSDs (Fig. 4j–l). Whereas the CSD for HOR-11-01B is kinked, suggesting that there is an excess of large crystals (Fig. 4j), CSDs for SKU-11-01B and SKU-11-02A are straight (Fig. 4k and l). However, olivine CSDs are not well determined because of the small number of crystals available for the calculations (110–396). Furthermore, olivine CSDs are truncated at much smaller crystal sizes than the maximum crystal sizes observed in thin sections (~1 mm in contrast to a maximum observed crystal size of 4 mm). This indicates that the area of a single thin section is insufficient to represent the full size distribution of olivine macrocrysts; large olivines are under-sampled. Plagioclase and clinopyroxene CSDs cover the full range of macrocryst sizes observed petrographically. It is therefore unlikely that a population of large clinopyroxenes is obscured by inadequate sampling.

ANALYTICAL METHODS

X-ray fluorescence spectrometry

A total of 32 whole-rock samples were analysed by X-ray fluorescence spectrometry (XRF) for major and trace elements. Samples were cut into 10–15 cm^3 blocks, washed in distilled water and dried prior to crushing in a steel jaw crusher and powdering in an agate ball mill at the University of Cambridge, UK. Fused glass discs and pressed powder pellets were prepared from rock powders and analysed using a Philips PW 2404 instrument at the University of Edinburgh, UK. A full description of sample preparation techniques has been given by Passmore *et al.* (2012). Major elements were measured on fused glass discs and trace elements (including Nb, Zr, Y, Sr, Zn, Cu, Ni and Cr) on pressed powder pellets following the analytical procedures of Fitton *et al.* (1998) with modifications by Fitton & Godard (2004).

Repeat analyses of the international standard BHVO-1 and two internal standards over many analytical sessions ($n = 136$) were used to estimate the accuracy of major element analyses. Accuracy of all major element analyses is estimated to be better than ±1·5%, except for Na_2O and P_2O_5, which overestimate literature values by 8·4% and 6·7% respectively (Govindaraju *et al.*, 1994). Accuracy of trace element analyses was estimated using measurements of international standards BIR-1, BCR-2 and BHVO-1 (Govindaraju *et al.*, 1994) during trace element analyses. Accuracy of trace element analyses is estimated as ±1% using BIR-1 and BHVO-1, but up to 2% for more abundant trace elements (e.g. Zr and Sr) and up to ±7% for less abundant trace elements (e.g. U, Th and Rb) using BCR-2. Analytical precision, incorporating errors associated with sample powder heterogeneity and preparation, was estimated by preparing and measuring repeats of four samples. The 1σ relative precision is estimated to be better than ±5% for most major elements (SiO_2, Al_2O_3, FeO_t, MgO, CaO and Na_2O) and some trace elements (Zr, Nb and Y), but higher for TiO_2, K_2O and P_2O_5 (±5·8%, ±7·0% and ±7·4% respectively) as well as some trace elements (±25·0% for La, ±5·8% for Rb and ±28·6% for Pb). The 1σ relative errors for all elements analysed by XRF are provided in Table 2.

Table 2: Geochemical variability in whole-rock major and trace elements measured by XRF

	$\bar{x}$	σ_o	σ_r	σ_t	σ_t/σ_r	% 1σ
SiO_2 (wt %)	48·68	0·38	0·19	0·33	**1·73**	0·39
TiO_2	1·34	0·17	0·09	0·14	**1·70**	6·35
Al_2O_3	17·24	1·64	0·47	1·57	**3·30**	2·75
FeO_t	9·73	1·03	0·37	0·96	**2·62**	4·78
MnO	0·17	0·02	0·05	–	–	28·81
MgO	6·97	0·40	0·05	0·40	**8·26**	0·69
CaO	12·98	0·43	0·21	0·38	**1·81**	1·60
Na_2O	1·68	0·12	0·02	0·12	**6·18**	1·17
K_2O	0·15	0·02	0·01	0·01	1·12	8·30
P_2O_5	0·11	0·02	0·01	0·01	1·19	8·71
La (ppm)	*2·35*	*1·00*	*0·97*	*0·23*	*0·23*	*41·31*
Ce	*15·67*	*1·92*	*0·77*	*1·76*	***2·29***	*4·92*
Nd	*10·76*	*1·55*	*0·65*	*1·40*	***2·15***	*6·06*
Nb	7·19	1·01	0·09	1·00	**10·97**	1·27
Zr	80·26	10·82	0·45	10·81	**23·87**	0·56
Y	23·44	3·16	0·11	3·16	**28·55**	0·47
Sr	153·85	4·26	0·18	4·25	**24·11**	0·11
Rb	3·18	0·54	0·20	0·50	**2·50**	6·34
Zn	84·70	11·04	0·47	11·03	**23·44**	0·56
Cu	109·01	13·38	0·50	13·37	**26·80**	0·46
Ni	86·62	3·81	0·67	3·75	**5·61**	0·77
Cr	247·06	16·16	3·30	15·82	**4·80**	1·34
V	286·41	35·72	1·31	35·69	**27·22**	0·46
Ba	33·65	6·23	1·70	6·00	**3·53**	5·05
Sc	41·41	4·73	0·65	4·68	**7·22**	1·57
Zr/Y	3·42	0·05	0·04	0·03	0·85	1·05
Nb/Zr	0·09	0·00	0·00	0·00	1·20	1·67

Bold indicates where signal-to-noise exceeds the threshold for statistical significance at the 99% confidence level of 1·61. Italics indicate elements that were analysed with greater precision by ICP-MS. $\bar{x}$, mean of samples; σ_o, observed standard deviation from the mean of samples; σ_r, repeat standard deviation based on multiple repeat analyses; σ_t, true standard deviation; σ_t/σ_r, signal-to-noise ratio; % 1σ, percentage 1σ relative precision.

Inductively coupled plasma mass spectrometry

All samples analysed by XRF were also analysed for trace elements by inductively coupled plasma mass spectrometry (ICP-MS) using a Perkin Elmer Elan DRCII instrument at the University of Cambridge, UK. From each powdered sample, 0·1 g of powder was dissolved at 120°C for 24 h in Teflon vials containing 1 ml 16N QD HNO_3 and 4 ml 48% HF. When complete digestion had been achieved, HF was removed by progressive evaporation, with samples topped up three times using 1 ml 16N QD HNO_3. When evaporation had been completed, 16N QD HNO_3 was added until a volume of 2·5 ml had been achieved. Solutions were diluted to 3·5% HNO_3 prior to running on the ICP-MS system.

The international standard NIST610 was used to calibrate the instrument (Jochum *et al.*, 2011). Blanks, international basaltic standards BIR-1 and BCR-2G and an in-house depleted basalt standard Hal-SN05 were analysed alongside the samples to estimate accuracy, which was generally better than ±5%, and always better than ±10%, relative to BIR-1 and BCR-2G (Jochum *et al.*, 2005). Analytical precision, including errors associated with sample dissolution and evaporation, was estimated by preparing 10 repeats of sample HOR-11-01 and running them alongside the other samples. The 1σ relative errors are ±3·5–5% for the majority of trace elements, including the rare earth elements (REE), and are reported in Table 3.

Electron probe microanalysis

Major element compositions of macrocrysts and matrix glasses were determined by electron probe microanalysis (EPMA) using a Cameca SX100 instrument at the University of Cambridge, UK. Matrix glass analyses were performed using a spot size of 10 μm, an operating potential of 15 kV and a beam current of 6 nA. Crystal analyses were performed with an operating potential of 15 kV and a beam current of 10 nA. A spot size of 5 μm was used for plagioclase analyses to minimize Na mobilization. A focused beam was used for olivine, clinopyroxene and chromite. Counting times were as follows: 20 s for major elements in glass and crystals, apart from Ti, which was counted for 60 s, and Na, which was counted for 10 s; 30 s for trace elements in crystals; and 60 s for P, Cr, Mn and Ni in glass. Standards were as follows: jadeite for Na, periclase for Mg, Si glass for Si, K-feldspar for K, rutile for Ti, fayalite for Fe, corundum for Al, apatite for P, and pure metals for Cr, Mn and Ni. Most analyses returned totals of 98·5–100·5 wt %. Samples with totals outside this range or inappropriate stoichiometry were discarded.

Crystal compositions are summarized throughout as follows: anorthite content for plagioclase [An = 100 × atomic Ca/(Ca + Na)], magnesium number for clinopyroxene [Mg# = 100 × atomic Mg/(Mg + Fe^{2+})], forsterite content for olivine [Fo = 100 × atomic Mg/(Mg + Fe^{2+})] and chromium number for chromite [Cr# = 100 × atomic Cr/(Cr + Al)]. Repeat analyses of standards were used to determine the precision of An, Mg# and Fo measurements. Anorthite content in the Anorthite55 standard was determined with a precision of ± 1·00 mol % (2σ, $n = 40$). Forsterite content of the St. John's Island Olivine standard was determined with a precision of ± 0·46 mol % (2σ, $n = 27$). Precision of clinopyroxene Mg# was similar to the precision of olivine forsterite content.

Table 3: Geochemical variability in whole-rock trace elements measured by ICP-MS

	$\bar{x}$	σ_o	σ_r	σ_t	σ_t/σ_r	% 1σ
La (ppm)	5·38	0·69	0·19	0·66	**3·46**	3·55
Ce	13·46	1·74	0·50	1·66	**3·31**	3·74
Pr	2·01	0·26	0·07	0·25	**3·50**	3·51
Nd	9·79	1·25	0·36	1·20	**3·36**	3·65
Sm	2·87	0·38	0·12	0·36	**3·07**	4·08
Eu	1·07	0·12	0·04	0·11	**2·66**	3·83
Gd	3·61	0·45	0·13	0·43	**3·41**	3·48
Tb	0·62	0·08	0·02	0·07	**3·25**	3·67
Dy	3·92	0·49	0·14	0·48	**3·52**	3·45
Ho	0·80	0·10	0·03	0·09	**2·74**	4·23
Er	2·31	0·29	0·08	0·28	**3·72**	3·30
Tm	0·34	0·04	0·01	0·04	**3·74**	3·25
Yb	2·10	0·26	0·08	0·25	**3·14**	3·79
Lu	0·31	0·04	0·01	0·04	**3·30**	3·57
Nb	*7·01*	*0·94*	*0·22*	*0·91*	***4·11***	*3·16*
Zr	*77·40*	*10·58*	*3·28*	*10·06*	***3·07***	*4·23*
Y	*22·63*	*2·85*	*0·84*	*2·72*	***3·23***	*3·73*
Sr	*162·80*	*6·46*	*6·39*	*0·93*	*0·15*	*3·93*
Rb	*2·94*	*0·44*	*0·30*	*0·31*	*1·04*	*10·22*
Cu	*114·94*	*13·31*	*3·93*	*12·72*	***3·24***	*3·42*
Ni	*86·11*	*5·30*	*4·00*	*3·48*	*0·87*	*4·65*
Zn	*75·15*	*8·67*	*2·52*	*8·29*	***3·29***	*3·36*
Cr	*246·26*	*16·98*	*10·99*	*12·95*	*1·18*	*4·46*
V	*299·79*	*39·95*	*8·12*	*39·12*	***4·82***	*2·71*
Ba	*33·25*	*4·83*	*1·42*	*4·61*	***3·24***	*4·28*
Sc	*37·72*	*4·35*	*1·43*	*4·10*	***2·86***	*3·80*
Pb	*0·46*	*0·09*	*0·05*	*0·07*	*1·62*	*9·80*
Th	*0·44*	*0·06*	*0·01*	*0·06*	***4·07***	*3·24*
U	*0·13*	*0·02*	*0·01*	*0·02*	***3·36***	*3·84*
Zr/Y	3·42	0·16	0·15	0·05	0·34	4·43
Nb/Zr	0·09	0·00	0·00	–	–	2·88

Bold indicates where signal-to-noise exceeds the threshold for statistical significance at the 99% confidence level of 1·81. Italics indicate elements that were analysed with greater precision by XRF. $\bar{x}$, mean of samples; σ_o, observed standard deviation in samples; σ_r, analytical precision based on multiple repeat analyses; σ_t, true standard deviation; σ_t/σ_r, signal-to-noise ratio; % 1σ, percentage 1σ relative precision.

Laser ablation inductively coupled plasma mass spectrometry

Selected trace elements were measured in clinopyroxene macrocrysts and plagioclase-hosted melt inclusions by laser ablation inductively coupled plasma mass spectrometry (LA-ICP-MS) using a Perkin Elmer Elan DRCII instrument interfaced with a New Wave Research UP213 laser ablation system at the University of Cambridge, UK. A spot size of 120 μm was used for macrocryst analyses to maximize sample delivery to the mass spectrometer. Melt inclusions were analysed with 60–80 μm spots. A laser repetition rate of 10 Hz and laser power of ~1 mJ (10 J cm^{-1}) were used for the entire study. Total ICP-MS data acquisition lasted 50 s. For each spot the first 20 s was a gas blank, followed by 30 s of laser analysis. To allow the element signals to return to baseline levels before moving to the next spot, a 40 s gas rinse-out time was employed. NIST-610 (Jochum *et al.*, 2011) was used as the calibration standard and concentrations were calculated by normalizing Ca to Ca determined by EPMA. Matrix corrections were performed using repeat analyses of the international glass standard BIR-1 (Jochum *et al.*, 2005). Repeat analyses of the international glass standards NIST612 (Jochum *et al.*, 2011), BCR-2G (Jochum *et al.*, 2005) and GOR-128 (Jochum *et al.*, 2006) were used to estimate precision and accuracy. Most trace elements were determined with accuracy better than ±10% with respect to published values. Elements with recoveries outside this range were not used in subsequent calculations. The 1σ relative precision of REE and Sr measurements in clinopyroxene macrocrysts was estimated as ~10% based on repeat analyses within single crystal zones. Typical 1σ relative precisions of trace element measurements in melt inclusions were estimated as ±10–15% using repeat analyses of BIR-1, BCR-2G and GOR-128. GLITTER software (GEMOC, Australia) was used to process the raw data files containing the signal intensity versus time data (the output from the Elan software), allowing contaminated and unsatisfactory signals to be identified and excluded.

Secondary ion mass spectrometry

Selected trace elements were measured in plagioclase macrocrysts by secondary ion mass spectrometry (SIMS) using a Cameca IMS-4f instrument at the NERC Ion Microprobe Facility at the University of Edinburgh, UK. Measurements were made using a primary O^- ion beam with an accelerating potential of 10 kV, a beam current of 5 nA and a secondary accelerating voltage of 4500 V minus a 75 V offset. The following isotopes were measured for 10 cycles, with counting times in seconds in parentheses: ^{7}Li (5), ^{26}Mg (5), ^{30}Si (2), ^{31}P (5), mass 38·3 (1), ^{39}K (2), ^{42}Ca (2), ^{47}Ti (3), ^{85}Rb (5), ^{88}Sr (3), ^{89}Y (10), mass 130·5 (5), ^{138}Ba (6), ^{139}La (15), ^{140}Ce (10). Peak positions were verified before each analysis, and masses 38·3 and 130·5 were measured to determine backgrounds in each cycle, which were always sufficiently close to zero to be ignored. NIST-610 (Jochum *et al.*, 2011) was used as the calibration standard and concentrations were calculated by normalizing ^{30}Si to Si determined by EPMA. Absolute element concentrations were calculated using JCION-6 software. Correction factors were applied for each element of interest based on comparison of known ion yields relative to ^{30}Si

for plagioclase standards with those of glass standards (Hinton, 1990). Precision was estimated by repeat analysis of the SHF-1 plagioclase (Irving & Frey, 1984), and indicates that trace elements were determined with 1σ relative precision of better than ±5% for all elements except Y, which was determined with a precision of ±25%.

QEMSCAN®

QEMSCAN® images were produced for two thin sections (SKU-12-18 and SKU-12-14A) in collaboration with FEI. Mineral and texture mapping was carried out using a QEMSCAN 650F at FEI's Centre of Excellence in Brisbane, Australia. Typically 5–7 million X-ray spectra were collected during a 10 μm raster grid of the entire thin section surface, according to methods outlined by Gottlieb *et al.* (2000) and Pirrie *et al.* (2004). More detailed scans were carried out at higher spatial resolutions (5 and 2·5 μm) on areas of specific interest. Plagioclase zoning was resolved using plagioclase species identification protocol (SIP) compositions that took relative Ca and Na contents into account. Olivine zoning was resolved using relative Mg and Fe contents.

RESULTS

Whole-rock and matrix glass compositions

Signal-to-noise ratios in whole-rock samples

Signal-to-noise ratios, which are a measure of the total variability in a dataset compared with the analytical uncertainty, were calculated for all elements measured by XRF and ICP-MS using the method of Maclennan *et al.* (2003*b*). Signal-to-noise ratios (σ_t/σ_r) were estimated using the relationship $\sigma_t^2 = \sigma_o^2 - \sigma_r^2$, where σ_t is the true variation of a dataset, σ_o is the standard deviation of a dataset and σ_r is an estimate of the true analytical noise (σ_R), determined using repeat analyses of samples. The χ^2 distribution was used to determine whether σ_t/σ_r was statistically significant at a given confidence level for each element. Twelve repeats were used to estimate σ_r for XRF analyses, and 10 repeats for ICP-MS analyses. Sample variability was considered statistically significant at the 99% confidence level if $\sigma_t/\sigma_r > 1{\cdot}61$ for XRF data and $\sigma_t/\sigma_r > 1{\cdot}81$ for ICP-MS data.

Signal-to-noise ratios calculated for elements measured by XRF and ICP-MS are shown in Tables 2 and 3, respectively. Variability in most trace element and some major element concentrations is greater than can be accounted for by analytical noise alone. Nb, Zr Sr, V and Y have very high signal-to-noise ratios (≫10) when analysed by XRF. Although the variability in trace element concentrations is significant, variability in trace element ratios, such as Nb/Zr and Zr/Y, is not (Tables 2 and 3).

Major elements

Whole-rock and matrix glass major element compositions are shown in Figs 5 and 6. Whole-rock compositions were determined by XRF and matrix glass compositions by EPMA. Full datasets are supplied in Supplementary Data Electronic Appendices 3 and 4 respectively.

Matrix glasses form a tightly clustered group with a mean MgO content of ~7·4 wt %. An average Mg# of 53 is calculated assuming melt $Fe^{3+}/\Sigma Fe \sim 0{\cdot}1$. Measured values of $Fe^{3+}/\Sigma Fe$ in Iceland basalts lie between 0·08 (Breddam, 2002) and 0·132 (Óskarsson *et al.*, 1994) and thus 0·1 represents a good approximation (Maclennan, 2008). Matrix glasses fall within the olivine tholeiite field of silica saturation based on CIPW norms, and are amongst the most primitive melt compositions known from the EVZ (see Hansen & Grönvold, 2000; Zellmer *et al.*, 2008; Passmore, 2009; Moune *et al.*, 2012; Neave *et al.*, 2013).

The MgO content of whole-rock samples ranges from 6·38 to 7·84 wt% (Fig. 5). MgO correlates positively with SiO_2, FeO_t and TiO_2 and negatively with Al_2O_3 and CaO. This positive correlation between MgO and TiO_2 contrasts with the negative correlation observed between these elements in tholeiitic matrix glasses from across the EVZ (Thordarson *et al.*, 2003). Whole-rock compositions do not overlap with the matrix glasses, except in the case of SiO_2 (Fig. 5a). Whole-rocks (Mg# ~ 56–61) have higher Mg# than the matrix glasses (Mg# ~ 53). Whole-rock Mg#, perhaps unexpectedly, correlates negatively with MgO (Fig. 6).

Trace elements

Whole-rock trace element variations are summarized in Fig. 7. Full XRF and ICP-MS datasets are supplied in Supplementary Data Electronic Appendix 3. All trace elements considered in subsequent discussions were measured by XRF, apart from the REE, which were measured by ICP-MS.

Trace element concentrations vary significantly between whole-rock samples (Fig. 7), which is reflected in large signal-to-noise ratios (Tables 2 and 3). Trace element ratios sensitive to variability in mantle melt composition do not, however, show significant variability at the 99% confidence level. For example, whole-rock Zr/Y is restricted to 3·32–3·52, which is considerably less than the range recorded in olivine-hosted melt inclusions from the same samples (2·01–5·17; Neave *et al.*, 2014). This suggests that any original parental melt heterogeneity has been homogenized by melt mixing before eruption (Rhodes *et al.*, 1979; Maclennan, 2008). In contrast to most trace elements, such as Zr and Nb (Fig. 7a and b), Sr and Ni correlate negatively with Y (Fig. 7c and d).

Hyaloclastite samples have similar compositions to pillow lavas, indicating that the magma source did not

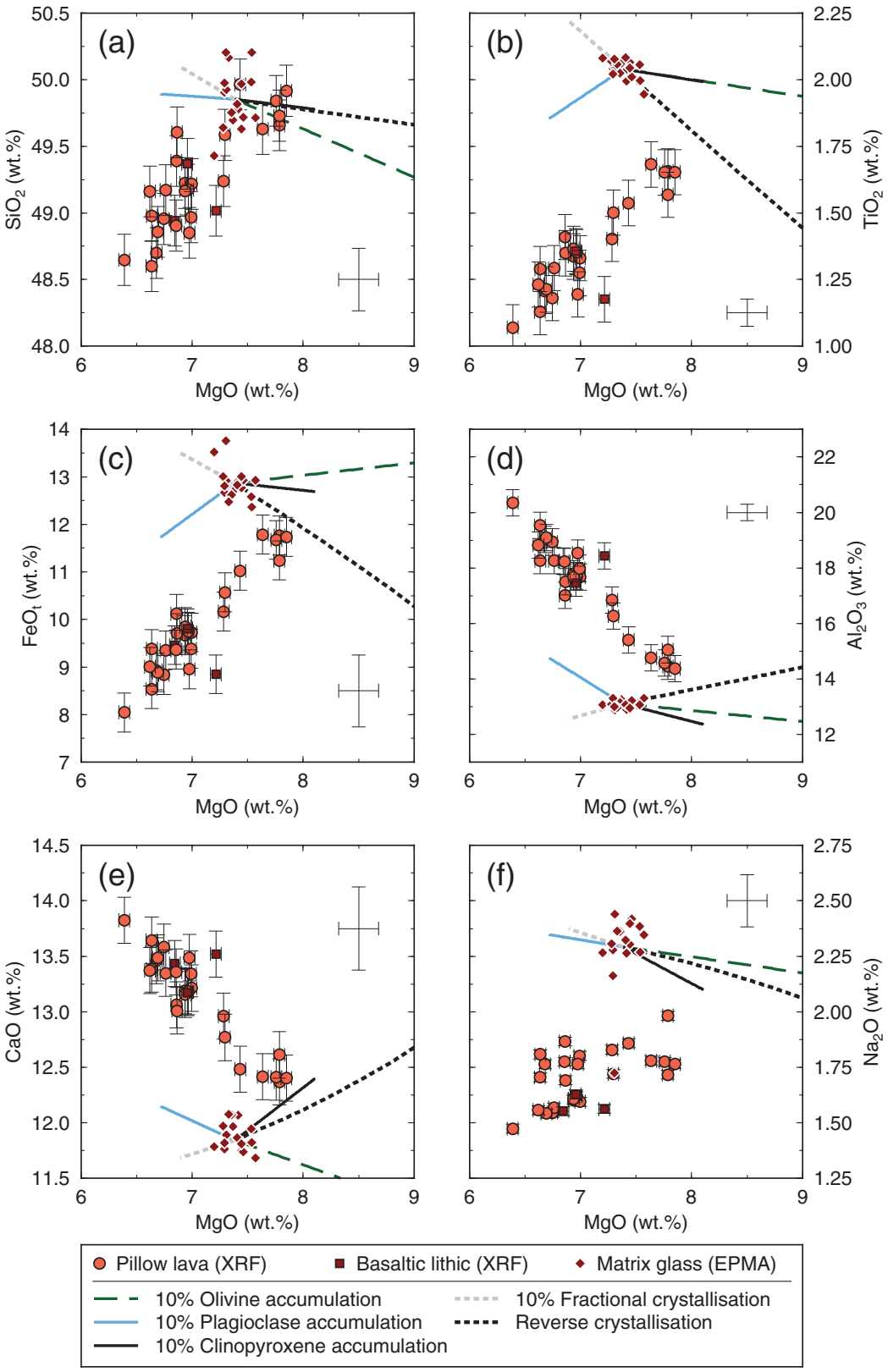

Fig. 5. Major element variations within Skuggafjöll whole-rocks and matrix glasses. The 1σ error bars are shown for each whole-rock sample and 1σ error bars for matrix glasses are shown as a separate error bar. Lines radiating from the average matrix glass composition show the effects of accumulating 10% plagioclase (pale blue), 10% clinopyroxene (black) and 10% olivine (dashed green). Paths illustrating how the matrix glass composition changes as a function of gabbro removal (fractional crystallization) and addition (reverse crystallization) are shown as dotted grey and dotted black lines respectively.

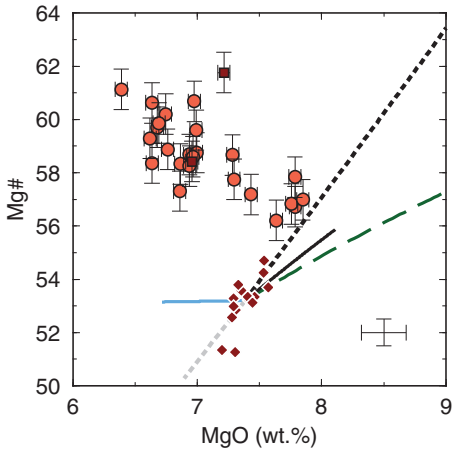

Fig. 6. Variation of Mg# with MgO wt % within Skuggafjöll whole-rocks and matrix glasses. Symbols and lines are as in Fig. 5. The negative correlation between MgO and Mg# should be noted.

change through the course of the eruption. Extensive hydration of hyaloclastite whole-rock samples, leading to loss on ignition (LOI) values of up to 8·4 wt %, did not affect trace element chemistry beyond simple dilution.

The trace element content of matrix glasses determined by LA-ICP-MS is presented on a multi-element diagram (Fig. 8). Data are normalized to the depleted MORB mantle (DMM) composition of Workman & Hart (2005) and are plotted alongside matrix glass and olivine-hosted melt inclusion compositions determined by SIMS (Neave *et al.*, 2014). Although there is some disparity between LA-ICP-MS and SIMS data, they lie within 1σ of each other (5–10%). The full LA-ICP-MS dataset is provided in Supplementary Data Electronic Appendix 5.

Element correlations

Cross-correlation matrices provide a way to check the quality and reproducibility of data between different analytical methods (Passmore *et al.*, 2012). A cross-correlation matrix for most elements measured in whole-rock samples is provided in Supplementary Data Electronic Appendix 6. The majority of trace elements and minor elements (i.e. TiO_2, MnO, K_2O and P_2O_5) correlate very strongly with each other ($r > 0{\cdot}9$), whether analysed by XRF or by ICP-MS, indicating good reproducibility between the two techniques. FeO_t also correlates strongly with most elements ($r > 0{\cdot}85$), but less so with MgO and SiO_2 ($r > 0{\cdot}75$). Na_2O and Ba correlate well with each other ($r = 0{\cdot}77$), but much less well with other elements (generally $r < 0{\cdot}5$). However, Al_2O_3, CaO, Sr and Ni behave very differently from all other elements: Al_2O_3, CaO and Sr correlate strongly with each other ($r > 0{\cdot}89$), but negatively with almost all other elements apart from Ni, with which they correlate modestly ($r \sim 0{\cdot}5$).

Principal component analysis (PCA; e.g. Albarède, 1996; McKenzie & O'Nions, 1998) illustrates that almost all of the variability in the whole-rock dataset is correlated: 99·4% of dataset variance can be explained by the first principal component alone. The first principal component correlates strongly and positively with all elements apart from Al_2O_3, CaO, Sr and Ni, with which it correlates strongly and negatively. The second principal component correlates moderately with Na_2O and Ba, but not with any other elements.

Macrocryst compositions and zonation

Macrocryst major elements

Macrocryst compositions are summarized in Fig. 9, where each point represents the mean of approximately three analyses within a single macrocryst zone. Plagioclase macrocrysts have compositions in the range $An_{70-90{\cdot}5}$, clinopyroxene macrocrysts have compositions in the range $Mg\# = 72-84$ and olivine macrocrysts have compositions in the range Fo_{75-87}. Kernel density estimations (KDEs) calculated using the method of Rudge (2008) for plagioclase and olivine are strongly bimodal, whereas the KDE for clinopyroxene is unimodal.

Spatial distributions of macrocryst compositions are shown in QEMSCAN® images of SKU-12-18 and SKU-12-14A (Figs 10 and 11, respectively). SKU-12-18 (Fig. 10) has a largely glassy matrix that is represented by a uniform colour (orange). Part of a large glomerocryst is present at the left of the image (marked 'A'). Within this glomerocryst the high-anorthite core of a large plagioclase (dark blue) abuts directly against the high-forsterite core of a large olivine macrocryst (dark khaki). Similar associations are observed in the centre of the image, where both chromite (black) and high-anorthite plagioclase are observed as inclusions within a high-forsterite olivine (marked 'B'). High-anorthite and high-forsterite compositions are never in contact with the groundmass, but are separated from the groundmass by rims of low-anorthite plagioclase and low-forsterite olivine. Small, low-anorthite and low-forsterite content macrocrysts are often associated with clinopyroxene macrocrysts (green).

The relationship between clinopyroxene and other macrocryst phases is more clearly observed in the image of SKU-12-14A (Fig. 11). Very small grains of olivine, plagioclase and clinopyroxene in the groundmass of SKU-12-14A illustrate this sample's higher degree of groundmass crystallinity compared with SKU-12-18. Clinopyroxene is observed in ophitic arrangement with low-anorthite plagioclase in a small glomerocryst towards the bottom right of the image (marked 'B'). The glomerocryst is further surrounded by small, low-forsterite olivine grains. Towards the top left of the image a number of small clinopyroxene grains are observed within the low-anorthite

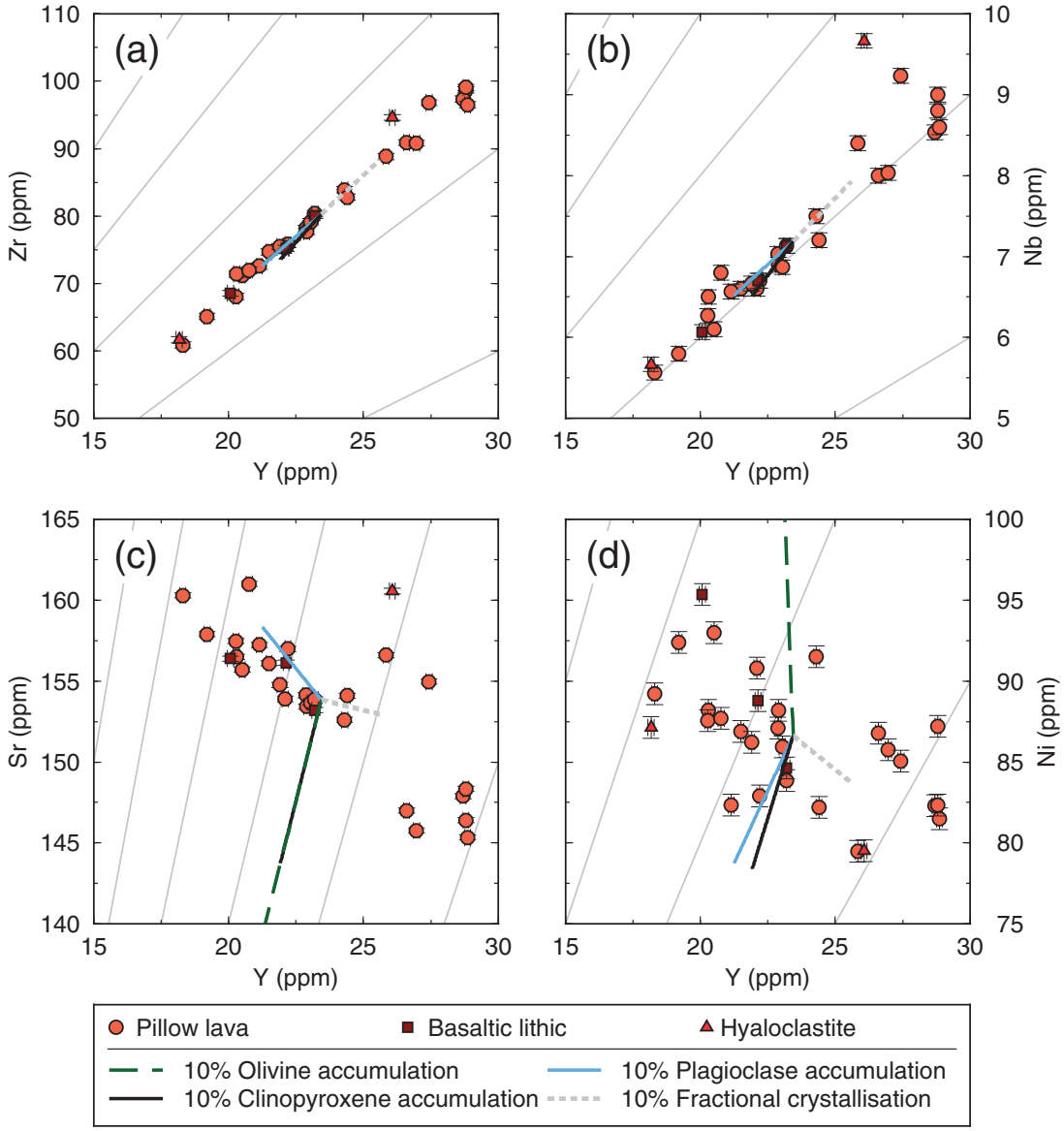

Fig. 7. Trace element variations within Skuggafjöll whole-rock samples. Pale grey lines show lines of constant element ratio.

rim of a plagioclase macrocryst with a small, high-anorthite core (marked 'A').

High anorthite contents ($An_{>83}$) occur in only the cores of large, low aspect ratio plagioclase macrocrysts. Low anorthite contents ($An_{<79}$) occur in the rims of large plagioclase macrocrysts and throughout small, high aspect ratio plagioclase macrocrysts. The average matrix glass composition is in equilibrium with an anorthite content of $An_{70·8}$ according to equation (33) of Namur *et al.* (2011*b*), which lies within the range of low-anorthite analyses (Fig. 9). High forsterite contents ($Fo_{>84}$) occur in only the cores of large (>500 μm) olivine macrocrysts that are often associated with high-anorthite plagioclase. Low forsterite contents ($Fo_{<82}$) occur in the rims of large olivine macrocrysts and throughout small (<500 μm) macrocrysts. Assuming $K_{dFe-Mg}^{ol-liq} = 0·3$ (Roeder & Emslie, 1970), the average matrix glass composition is in equilibrium with $Fo_{79·2}$, which is similar to the lowest forsterite contents measured (Fig. 9). Clinopyroxene macrocrysts are associated with low-anorthite plagioclase and low-forsterite olivine, and occur both around the edges of large glomerocrysts and in small ophitic glomerocrysts. Using a $K_{dFe-Mg}^{cpx-liq}$ value of 0·28 calculated from Wood & Blundy (1997), the average matrix glass composition is in equilibrium with Mg# = 80·3 clinopyroxene, which lies towards the lower end of the range of measured clinopyroxene

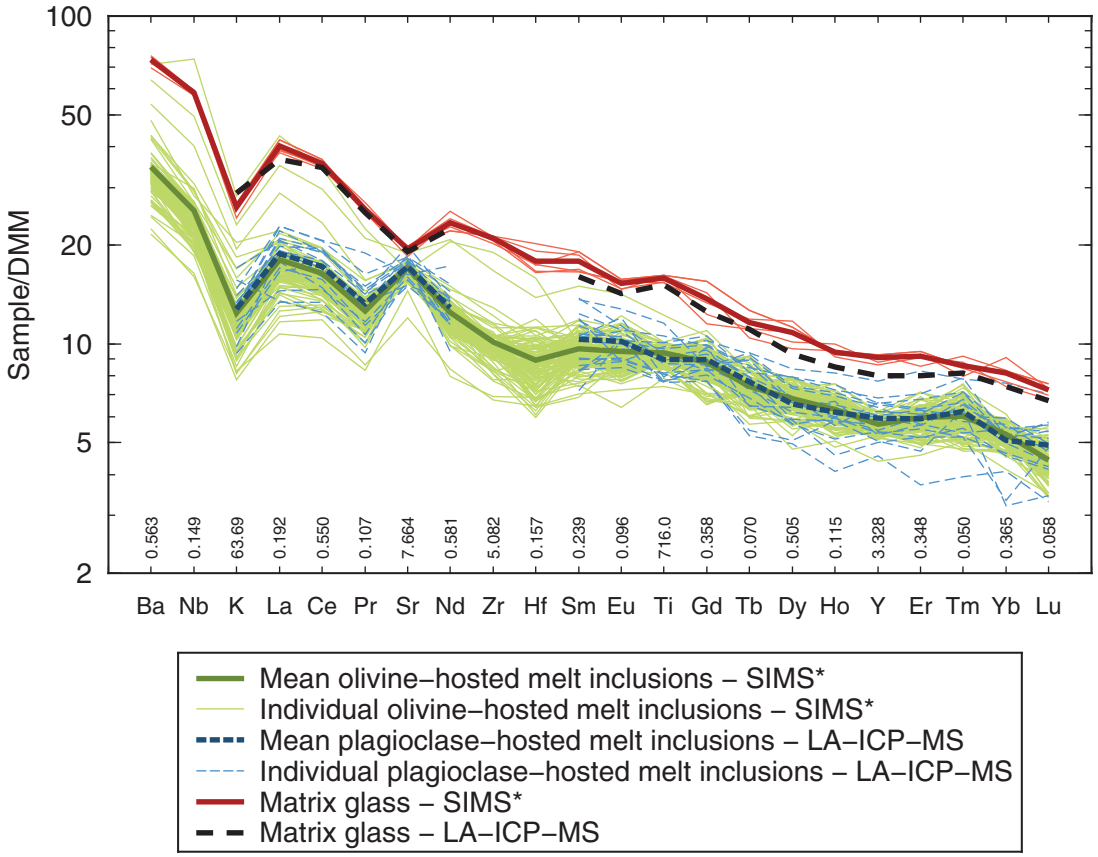

Fig. 8. Depleted MORB mantle-normalized (DMM; Workman & Hart, 2005) multi-element diagram for melt inclusions and matrix glasses from Skuggafjöll. Normalization values are shown along the base of the plot. Olivine-hosted melt inclusions and matrix glasses measured by SIMS from Neave *et al.* (2014), which are marked * in the legend, are shown alongside plagioclase-hosted melt inclusions and matrix glasses measured by LA-ICP-MS. Element concentrations measured by SIMS and LA-ICP-MS are generally reproduced within analytical precision. Although both olivine-hosted and plagioclase-hosted melt inclusions exhibit scatter in their trace element contents, the mean compositions of the two inclusion suites are very similar.

compositions (Fig. 9). Chromite grains occur as inclusions within high-anorthite plagioclase and high-forsterite olivine, and can be classified as Mg-Al-chromites (Cr# ~ 42–54).

Macrocryst trace elements

The bimodality of anorthite content in plagioclase macrocrysts is also reflected in their trace element contents (Fig. 12a and b); TiO_2 and FeO_t negatively correlate with anorthite content. High-anorthite plagioclase generally contains $0{\cdot}02 \pm 0{\cdot}01$ (1σ) wt % TiO_2 whereas low-anorthite plagioclase contains $0{\cdot}04 \pm 0{\cdot}01$ (1σ) wt % TiO_2 at An_{79}, increasing to $0{\cdot}06 \pm 0{\cdot}01$ (1σ) wt % TiO_2 at An_{70} (Fig. 12a). High-anorthite plagioclase has an FeO_t content of $0{\cdot}45 \pm 0{\cdot}13$ (1σ) wt % and low anorthite plagioclase an FeO_t content of $0{\cdot}65 \pm 0{\cdot}13$ (1σ) wt % (Fig. 12b).

A wider range of trace elements were measured in a few plagioclase macrocrysts by SIMS. Although insufficient analyses were performed to comment on intra-zone variability, inter-zone compositional differences are highlighted (Fig. 12c and d). For example, low concentrations of Ba and Sr are found in high-anorthite cores of large plagioclase grains (~2·5 ppm and ~170 ppm respectively), whereas higher concentrations occur in low-anorthite rims (~6·5 ppm and ~205 ppm respectively). A single analysis in the low-anorthite core of a small macrocryst is indistinguishable from the composition present in rims of large macrocrysts. Full SIMS data are provided in Supplementary Data Electronic Appendix 7.

The TiO_2 content of clinopyroxenes correlates well with Mg#, and increases from ~0·4 wt % at Mg# = 84 to ~0·9 wt % at Mg# = 80 (Fig. 13a). The Cr_2O_3 content of clinopyroxenes is highly variable at a constant Mg# (e.g. 0·2–0·9 wt % at Mg# = 82). Cr_2O_3 and Al_2O_3 correlate positively in clinopyroxene cores (Fig. 13b), indicating that the Cr content of the clinopyroxenes is strongly controlled by the uptake of cations during the development of sector zonation, and is not simply related to melt composition (Nakamura, 1973).

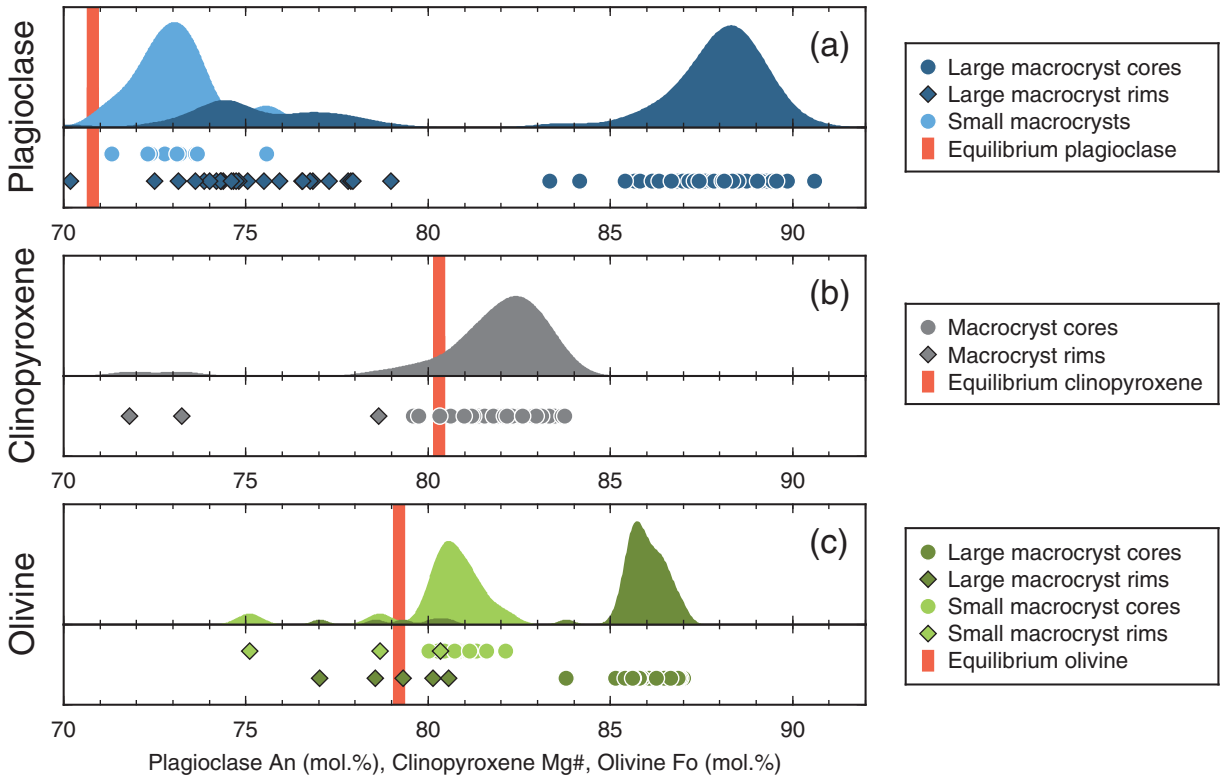

Fig. 9. Summary of macrocryst compositions determined by EPMA. For plagioclase and olivine, data are divided into populations of large and small macrocrysts shown in dark and light shading respectively. Large plagioclase macrocrysts have low aspect ratios (length/width ~1·5) and small plagioclase macrocrysts have high aspect ratios (length/width > 2). Each data point in the lower part of each figure represents the average of 2–4 analyses in the macrocryst zone of interest. The upper part of each figure shows kernel density estimations (KDEs) for each macrocryst population using the method discussed by Rudge (2008). Bimodality is observed in both plagioclase (a) and olivine (c) compositions, but not in clinopyroxene (b) compositions. The vertical bars show macrocryst compositions in equilibrium with the average matrix glass composition calculated using the model of Namur *et al.* (2011*b*) for plagioclase, Wood & Blundy (1997) for clinopyroxene, and a constant K_{dFe-Mg}^{ol-liq} of 0·3 for olivine.

DMM-normalized REE contents of clinopyroxene macrocrysts are shown in Fig. 13c. Variations in clinopyroxene REE and Y concentrations are significant at the 99% confidence level. Incompatible trace element ratios between elements determined with high precision (1σ relative precision of better than ± 10%), such as Ce/Yb and Ce/Y, also show significant variability.

Plagioclase-hosted melt inclusion compositions

Plagioclase-hosted melt inclusions are located in high-anorthite cores (An_{86-89}) and preserve primitive melt compositions ($Mg\# = 64 \pm 2$) in equilibrium with Fo_{84-87} olivines. Although the CaO, Na_2O, Al_2O_3 and SiO_2 contents of plagioclase-hosted melt inclusions are affected by post-entrapment crystallization processes (Nielsen, 2011), Mg# should be unaffected because of the low concentration of MgO and FeO_t in plagioclase. Trace element contents of 17 plagioclase-hosted melt inclusions are summarized alongside trace element contents of 110 olivine-hosted melt inclusions from Neave *et al.* (2014) in Fig. 8. Although the LA-ICP-MS data are more noisy than the SIMS data, both suites of melt inclusions have similar mean compositions. The correspondence between mean compositions is best for elements measured with high precision, such as La, Ce, Sr and Y. Trace element ratios, such as Ce/Y, are also indistinguishable within the limits of analytical precision: mean $Ce/Y_{ol\text{-}hosted} = 0{\cdot}47 \pm 0{\cdot}010$ (1σ error) and mean $Ce/Y_{plg\text{-}hosted} = 0{\cdot}48 \pm 0{\cdot}012$ (1σ error).

DISCUSSION

Geochemical variability in Skuggafjöll whole-rock samples

Whole-rock samples are mixtures of quenched melt and macrocrysts, some of which may not have crystallized from the melt in which they are carried. Consequently, whole-rock compositions are controlled by processes that affect the crystal content of the magma, such as crustal

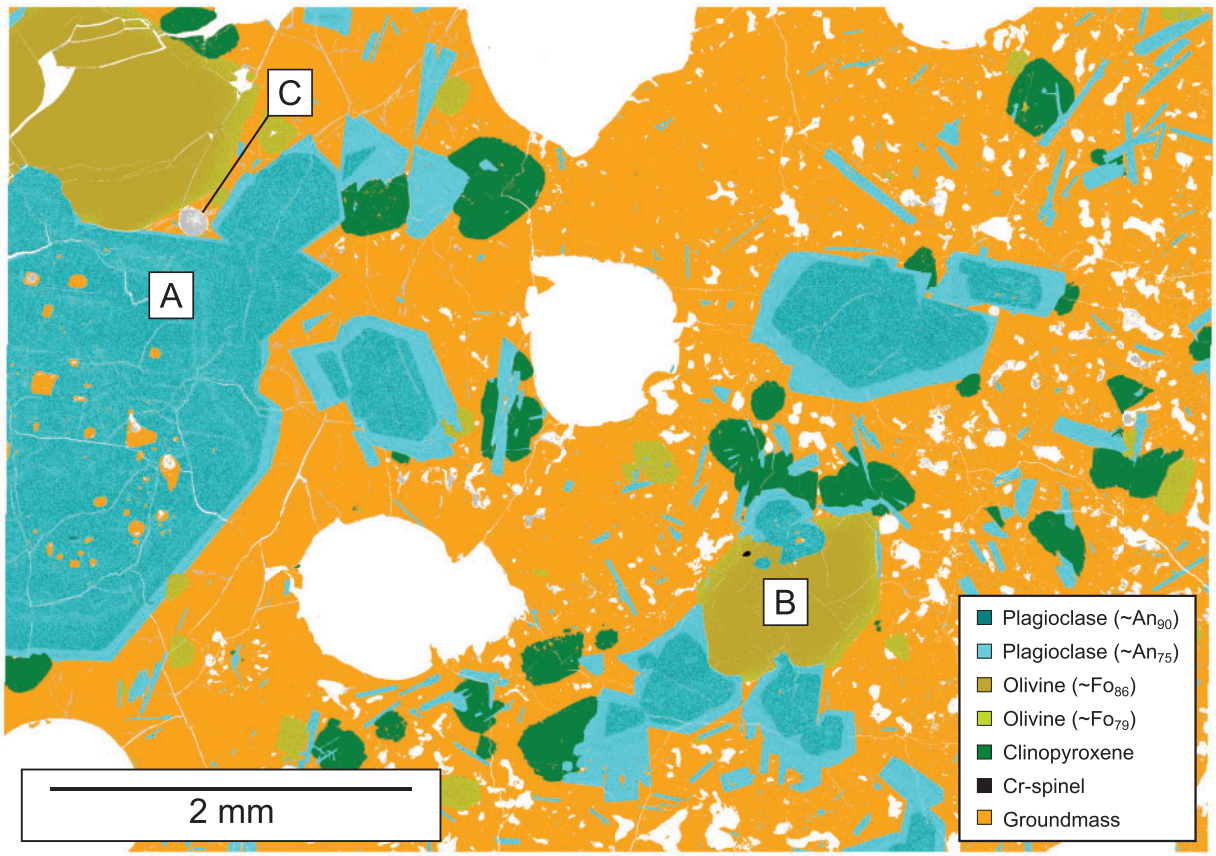

Fig. 10. QEMSCAN® image of SKU-12-18. Both plagioclase and olivine exhibit compositional bimodality. High-anorthite and high-forsterite cores of large macrocrysts are shown in dark blue and dark khaki respectively and define a primitive assemblage (along with minor chromite). Lower anorthite and forsterite contents are shown in paler shades of blue and khaki. Alongside clinopyroxene, shown in green, these low-anorthite plagioclases and low-forsterite olivines define an evolved assemblage. Clinopyroxene is never in contact with primitive plagioclase or olivine. The difference in morphology between stubby, large, high-anorthite plagioclase and elongate, small, low-anorthite plagioclase is particularly clear. This sample has a glassy groundmass, reflected in a uniform orange colour. White spaces are vesicles. Part of a large glomerocryst is marked 'A'. Chromite and high-anorthite plagioclase inclusions within high-forsterite olivine are marked 'B'. A complex interstitial space that is likely to have contained mush liquid is marked 'C'.

assimilation or crystal settling, as well as those that affect melt composition, such as fractional crystallization, crystal dissolution or mixing.

Paths showing gabbro addition and removal are shown in Figs 5–7 as dotted black and grey lines, respectively. Gabbro removal paths assume 10% crystallization of an assemblage containing plg:cpx:ol in the ratio 11:6:3. Major element gabbro addition paths were calculated using the method of equilibrium macrocryst selection as described by Neave *et al.* (2013). Macrocryst trace element compositions that were not measured directly were estimated using appropriate partition coefficients: those of Blundy & Wood (1991), Bindeman & Davis (2000) and Bédard (2006) for plagioclase; those of Wood & Blundy (1997) and Hill *et al.* (2010) for clinopyroxene; those of Bédard (2005) for olivine. Partition coefficients were calculated at 1190°C and 0·5 kbar based on clinopyroxene–melt thermometry (Putirka, 2008) and melt inclusion entrapment pressures (Neave *et al.*, 2014).

Gabbro addition and removal paths lie at high angles to the arrays of whole-rock data in Figs 5–7. In particular, the negative correlation of Mg# with MgO in whole-rock samples cannot be explained by fractional crystallization involving the removal of ferromagnesian phases (Fig. 6). Strong negative correlations between Al_2O_3 and MgO (Fig. 5d), and Sr and Y (Fig. 7c) can nevertheless be explained by the addition or removal of plagioclase, as the Al_2O_3 content of plagioclase is much greater than that of the matrix glass or other macrocryst phases. However, neither plagioclase addition nor plagioclase removal can account for the negative correlations between Mg# and MgO (Fig. 6), and Ni and Y (Fig. 7d). These negative correlations are consistent with the addition or removal of Ni-rich olivine.

In addition to the inter-elemental correlations discussed above, correlations are also observed between the whole-rock compositions and macrocryst mass fractions determined by point counting (Fig. 14). Positive correlations

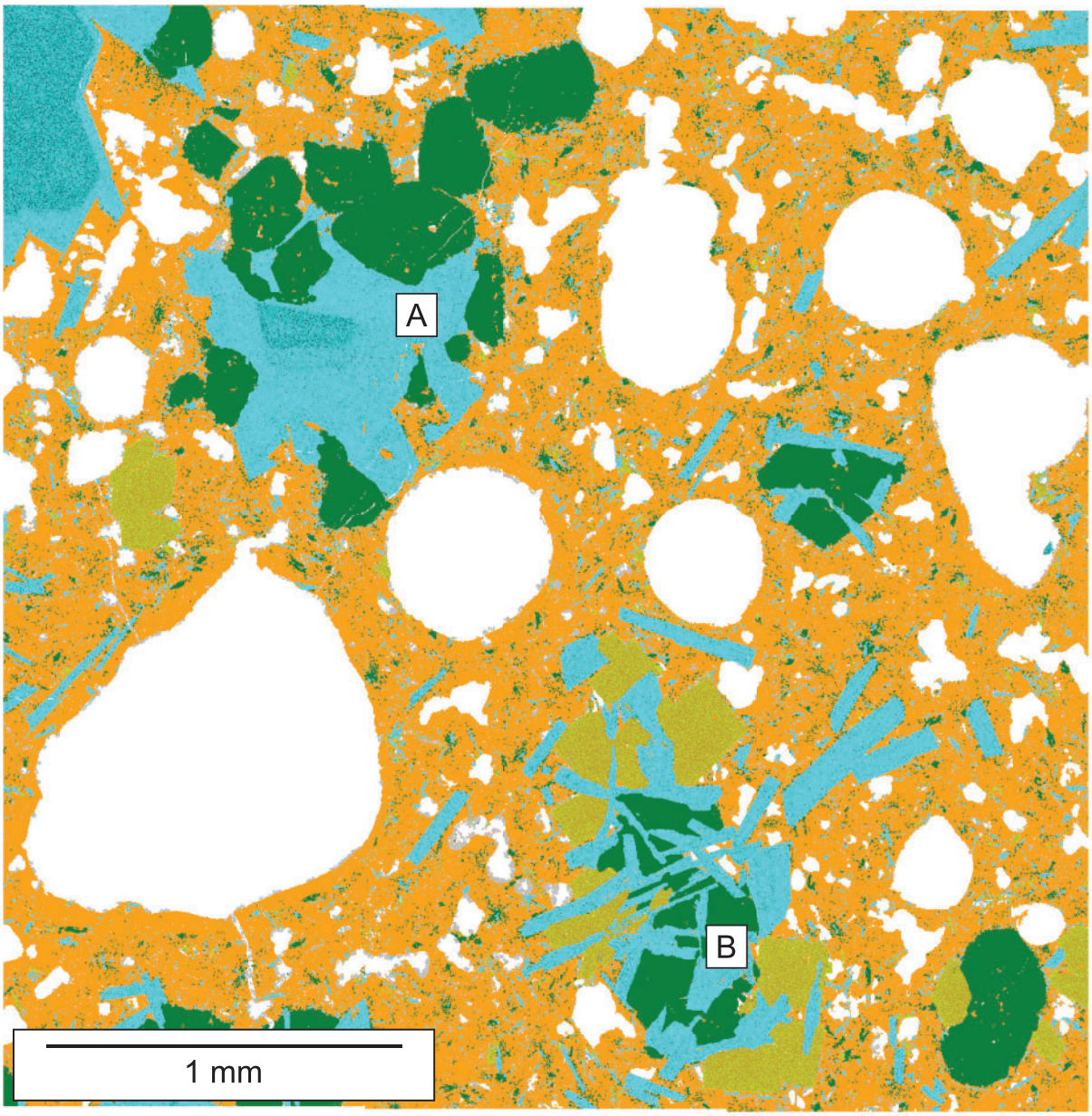

Fig. 11. QEMSCAN® image of SKU-12-14A. Colours are as for Fig. 10. Small glomerocrysts containing low-anorthite plagioclase and clinopyroxene in ophitic arrangement are shown in this image. The glomerocryst towards the top left is bimineralic, whereas that towards the bottom right contains low-forsterite olivine intergrown with clinopyroxene and low-anorthite plagioclase. The speckled appearance of the groundmass in this thin section results from the presence of microlites. A glomerocryst containing plagioclase and clinopyroxene in ophitic arrangement is marked 'A'. A gabbroic glomerocryst containing low-forsterite olivine is marked 'B'.

between both Sr and Ni and macrocryst mass fraction ($r = 0{\cdot}708$ and $r = 0{\cdot}385$ respectively) are consistent with the control of whole-rock geochemical variability by accumulation of Sr-rich plagioclase and Ni-rich olivine (Fig. 14b and d). Cr correlates negatively with macrocryst mass fraction (Fig. 14c; $r = -0{\cdot}502$), indicating that neither clinopyroxene nor chromite play a significant role in controlling geochemical variability in whole-rock samples. Sc, which partitions strongly into clinopyroxene, also correlates negatively with macrocryst mass fraction ($r = -0{\cdot}73$; Supplementary Data Electronic Appendix 8).

Constraining the phase proportions of accumulated macrocrysts

Fitting liquid lines of descent between primitive and evolved end-members using least-squares methods is an

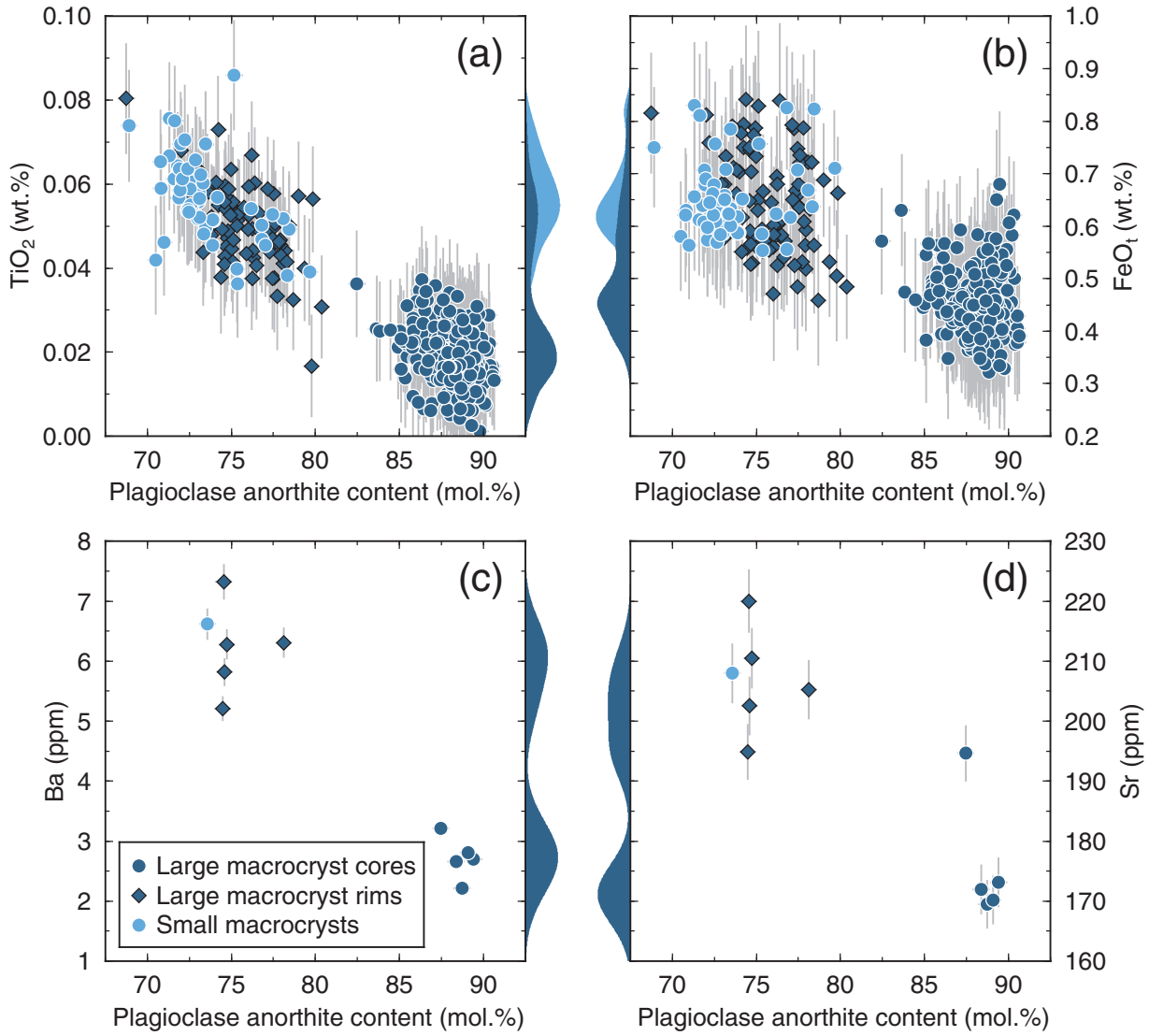

Fig. 12. Plots summarizing the trace element content of plagioclase macrocrysts from Skuggafjöll. Plagioclase anorthite content (mol %) = 100 × atomic Ca/(Na + Na). TiO_2 (a) and FeO_t (b) were measured by EPMA. Ba (c) and Sr (d) were measured by SIMS. Data are shown with 2σ error bars.

established technique for constraining the proportions of crystallizing phases in magmatic systems (Wright & Doherty, 1970). To avoid specifying end-members *a priori*, Maclennan *et al.* (2001) developed an analogous method whereby phase proportions were fitted to the principal component axes of a whole-rock major element dataset. This PCA-based method is readily adapted to studies of crystal accumulation, where principal component axes thus represent the addition or removal of different macrocryst assemblages.

The first principal component accounts for 99·4% of the total variance in whole-rock SiO_2, Al_2O_3, FeO_t, MgO and CaO contents at Skuggafjöll, and can be accounted for by addition or removal of an assemblage containing 89·3% plagioclase, 0·9% clinopyroxene and 9·8% olivine. The r.m.s. error of the least-squares fit is small (0·09), indicating that these phase proportions are well constrained. The second principal component, which accounts for 0·4% of the total variance, can be accounted for by addition or removal of a broadly gabbroic assemblage containing 39·8% plagioclase, 52·3% clinopyroxene and 7·9% olivine, also with a small r.m.s. error (0·09). Compositional variability in whole-rock samples is therefore controlled by the accumulation of variable amounts of a troctolitic assemblage containing plagioclase and olivine in an ~9:1 ratio. This ~9:1 ratio is significantly more plagioclase-rich than the plg:ol ~7:3 ratio expected during cotectic crystallization (Grove *et al.*, 1992). Clinopyroxene does not play a

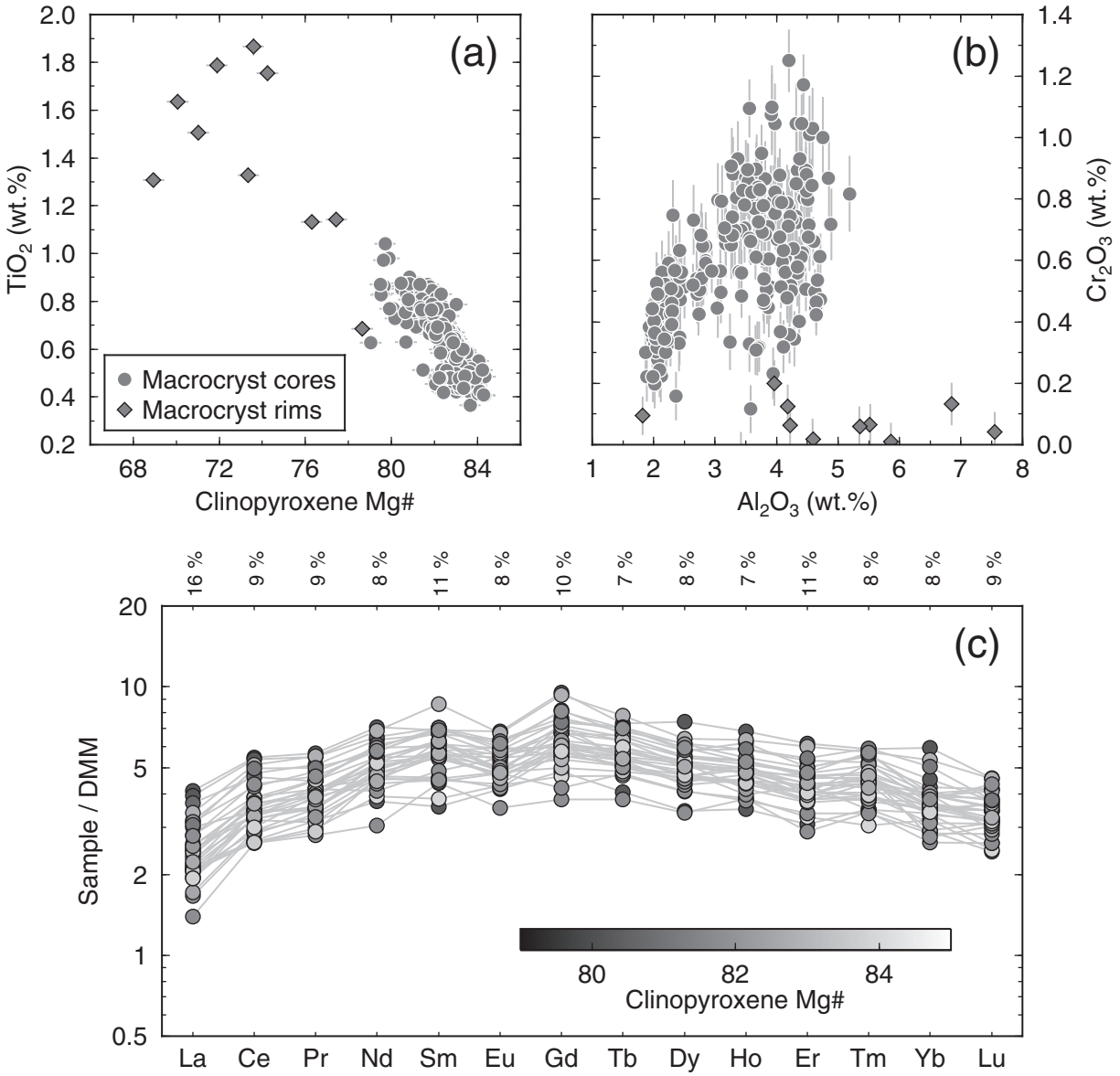

Fig. 13. Plots summarizing the trace element content of clinopyroxene macrocrysts from Skuggafjöll. Clinopyroxene Mg# = 100 × atomic Mg/(Mg + Fe^{2+}). TiO_2 (a), and Al_2O_3 and Cr_2O_3 (b) were measured by EPMA. (a) Anticorrelation between clinopyroxene Mg# and TiO_2 is controlled primarily by fractional crystallization processes. (b) The correlation of Al_2O_3 and Cr_2O_3 in clinopyroxene cores is primarily controlled by the effects of sector zoning (Nakamura, 1973). (c) REE measured by LA-ICP-MS are normalized to the depleted MORB mantle (DMM) composition of Workman & Hart (2005). The 1σ relative errors for each element are shown along the top of the plot.

significant role in controlling whole-rock variability; the identification of small amounts of clinopyroxene in the assemblage controlling the first principal component may be an artefact of the fitting procedure.

Phase proportions of accumulated macrocrysts were also estimated from point counting data. Although least-squares fitting of whole-rock data indicates that clinopyroxene does not play a significant role in controlling the variability of whole-rock samples, it is nevertheless present and must be accounted for in any complete petrogenetic model for Skuggafjöll. If clinopyroxene is assumed to have crystallized at the three-phase gabbro eutectic alongside plagioclase and olivine, it is then possible to distinguish eutectic macrocrysts from accumulated macrocrysts. Observations supporting the assumption of clinopyroxene formation during three-phase crystallization are discussed in a later section. Mass fractions of plagioclase and olivine from the eutectic assemblage were calculated from the mass fraction of clinopyroxene in each sample assuming a plg:cpx:ol ratio of 11:6:3. Mass fractions of accumulated

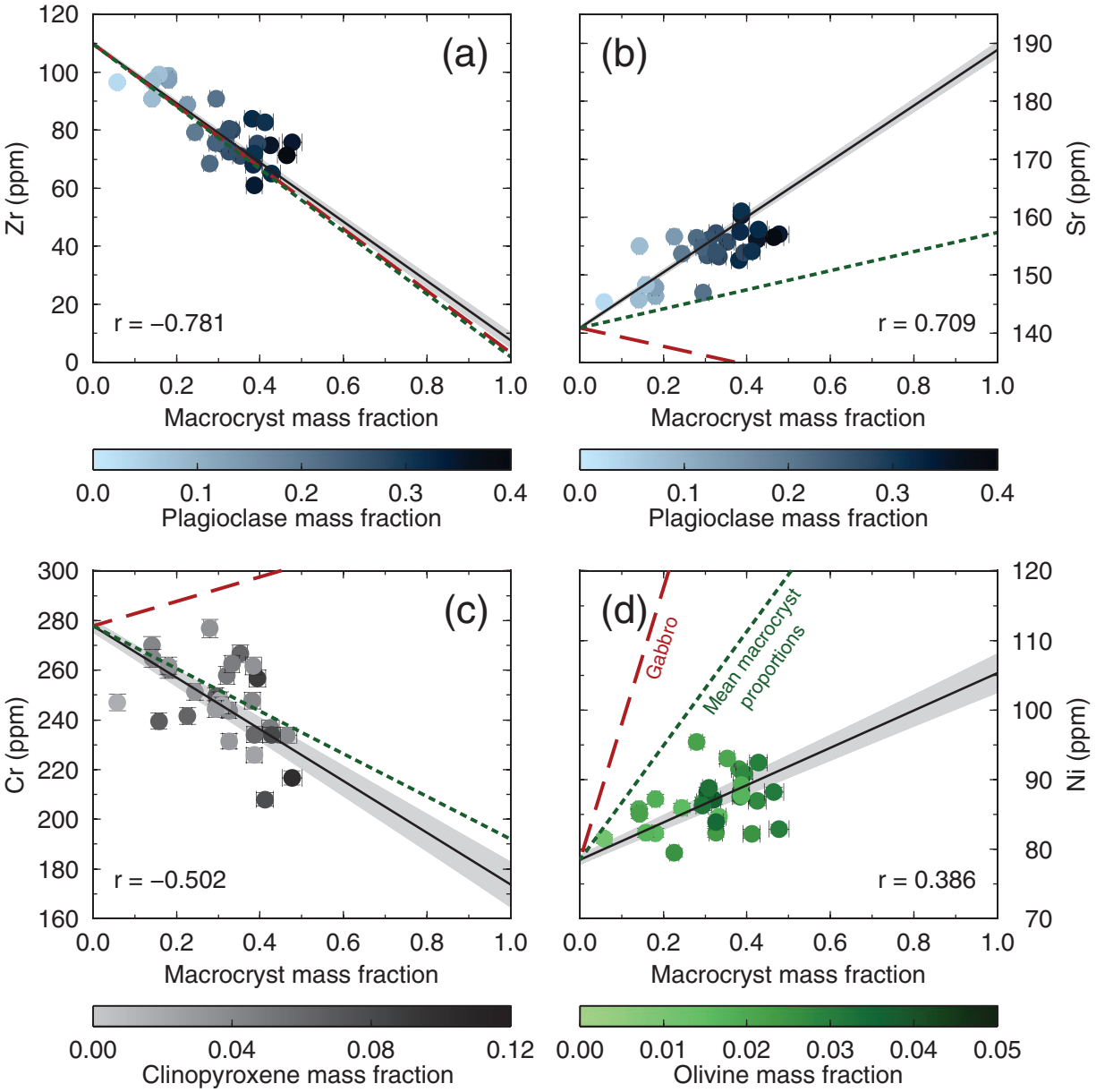

Fig. 14. Plots showing the relationship between mass fraction of macrocrysts and the concentration of key trace elements in Skuggafjöll whole-rock samples. The 1σ error bars are of similar magnitude to the symbols. The black line shows the results of linear regression taking account of errors (York, 1969), with 1σ error envelopes for linear regressions shown by grey fields. The correlation coefficient is shown in the bottom corner of each plot. The red dashed line shows the effect of adding a gabbroic assemblage to a melt composition taken as the intercept from regression of the data. The green dotted line shows the effect of adding the mean proportion of macrocrysts determined by point counting. Elements were chosen on account of their compatibilities: Zr (a) is incompatible in all macrocryst phases; Sr (b) is compatible in plagioclase; Cr (c) is compatible in clinopyroxene (and chromite); Ni (d) is compatible in olivine.

plagioclase and olivine were then calculated by subtracting the eutectic assemblage from the total macrocryst content of each sample.

Samples contain an average total macrocryst mass fraction of 30·9 ± 10·7% (1σ). Overall, 13·4 ± 5·8% (1σ) of this total macrocryst mass fraction can be accounted for by crystallization at the three-phase gabbro eutectic, leaving an average macrocryst mass fraction of 17·4 ± 10·1% (1σ). On average, this residual assemblage, assumed to represent accumulated macrocrysts, contains 93·7% plagioclase and 6·3% olivine. Although the calculated proportion of plagioclase in the accumulated material varies from 44 to 100% between samples, much of this variability is attributable to errors in point counting data.

Scatter on whole-rock variation diagrams (e.g. Fig. 5c) suggests that different samples have nevertheless accumulated slightly different proportions of plagioclase and olivine. The full range of whole-rock data can be accounted for by the accumulation of plagioclase and olivine in ratios between 1:0 and 8:1 (Supplementary Data Electronic Appendix 9). All samples have therefore experienced accumulation of plagioclase-dominated assemblages. No samples show geochemical evidence for accumulation of olivine-rich material. Furthermore, no samples show evidence for accumulation of material with cotectic proportions (plg:ol ~7:3).

The fraction of macrocrysts associated with three-phase eutectic crystallization varies less between samples than the mass fraction of macrocrysts associated with troctolite accumulation, implying that all samples have experienced similar extents of crystallization at the three-phase gabbro eutectic. A eutectic macrocryst mass fraction of ~13% is consistent with the extent of crystallization required to link matrix glass compositions with whole-rock samples (Figs 5 and 6). Both whole-rock geochemical variability and point counting systematics thus suggest that the Skuggafjöll magma crystallized in two stages. Records of two-stage crystallization will now be discussed to validate the assumptions made during the calculation of accumulated macrocryst mass fractions and to investigate the processes driving multi-stage petrogenesis.

Records of two stages of crystallization in the Skuggafjöll magma

Identification of macrocryst assemblages in QEMSCAN® images

Combined whole-rock and point counting systematics in Skuggafjöll lavas can be accounted for by crystallization of macrocrysts in two discrete stages. By understanding the spatial distribution of compositions within and between crystals it is possible to determine which macrocryst phases, and also which macrocryst zones, were in equilibrium at different stages of crystallization. The combination of compositional and textural information in QEMSCAN® images (Figs 10 and 11) allows two macrocryst assemblages to be defined: high-forsterite olivine and high-anorthite plagioclase, along with minor chromite, define a primitive assemblage, and low-forsterite olivine, low-anorthite plagioclase and clinopyroxene define an evolved assemblage. The troctolitic mineralogy of the primitive assemblage is consistent with the mineralogy of the accumulated material identified in the previous section. The gabbroic mineralogy of the evolved assemblage is consistent with formation during a second stage of crystallization that followed accumulation of the primitive assemblage. The primitive assemblage is far from being in equilibrium with the matrix glass, whereas the evolved assemblage is close to being in equilibrium with it and has almost certainly crystallized from it. By considering the trace element content of melts from which the macrocrysts crystallized, it is possible to determine whether the gap between primitive and evolved assemblages (Figs 9 and 12) corresponds to a step in the degree of melt evolution, or is also related to changes in parental magma source.

Melt inclusions in primitive macrocrysts

It is well established that melt inclusions hosted in primitive macrocrysts can preserve records of primitive melt variability; variability has been reported in melt inclusions hosted in forsteritic olivine (Sobolev & Shimizu, 1993; Gurenko & Chaussidon, 1995; Kamenetsky *et al.*, 1998; Sobolev *et al.*, 2000; Maclennan *et al.*, 2003*a*) and anorthitic plagioclase (Sinton *et al.*, 1993; Nielsen *et al.*, 1995; Sours-Page *et al.*, 2002; Adams *et al.*, 2011). Olivine-hosted and plagioclase-hosted melt inclusions are present at Skuggafjöll (Neave *et al.*, 2014; this work), and their trace element compositions are summarized in Fig. 8. Both melt inclusion suites show significant variability in trace element ratios that are fractionated substantially only during mantle melting: signal-to-noise ratios for Ce/Y measured in olivine-hosted and plagioclase-hosted melt inclusions are 3·71 and 1·54 respectively, and are above the threshold for significant variability at the 99% confidence level in their respective sample sets (Neave *et al.*, 2014). The mean composition of melt inclusions hosted in both phases is similar [$Ce/Y_{ol\text{-}hosted} = 0{\cdot}47 \pm 0{\cdot}010$ (1σ) and $Ce/Y_{plg\text{-}hosted} = 0{\cdot}48 \pm 0{\cdot}012$ (1σ)], indicating that high-forsterite olivine and high-anorthite plagioclase almost certainly crystallized from the same suite of primitive melts. Co-crystallization of olivine and plagioclase probably occurred along the low-pressure ol–plg cotectic (e.g. Grove *et al.*, 1992). It is important to note that Ce/Y_{melt} values measured in matrix glasses (0·65 and 0·71 by SIMS and LA-ICP-MS, respectively) are significantly more enriched in incompatible trace elements than the means of the melt inclusion populations. This difference in enrichment between primitive melt inclusions and the matrix glasses requires that the primitive and evolved assemblages crystallized from different primary melt distributions.

Melt inclusion major element compositions provide further confirmation that ~An_{88} plagioclase and ~Fo_{86} olivine crystallized from the same suite of melts. Although the Mg# content of olivine-hosted melt inclusions is strongly affected by post-entrapment modification (e.g. Danyushevsky *et al.*, 2002), Ca/Na, expressed throughout as an atomic ratio, should be little affected (Neave *et al.*, 2013). The Ca/Na of primitive olivine-hosted melt inclusions of Neave *et al.* (2014) is $3{\cdot}92 \pm 0{\cdot}21$ (1σ), a value consistent with those measured in matrix glasses from the incompatible trace element depleted Kistufell eruption that are in equilibrium with $An_{82–89}$ plagioclase (Breddam, 2002; Neave *et al.*, 2013).

Although the Ca/Na of plagioclase-hosted melt inclusions is subject to post-entrapment modification by crystallization or dissolution of plagioclase on inclusion walls, the Mg# content of melt inclusions should be comparatively unaffected. Whereas inclusions that have experienced post-entrapment crystallization show enrichments in MgO and FeO_t and depletions in Al_2O_3, changes in Mg# from post-entrapment crystallization are modest (Nielsen, 2011). Plagioclase-hosted melt inclusions from Skuggafjöll have an Mg# of 64 ± 2, which is the melt Mg# range predicted to be in equilibrium with Fo_{85-87} olivine (Neave *et al.*, 2014).

Both major and trace element contents of the melt inclusions thus corroborate the interpretation that high-forsterite olivine and high-anorthite plagioclase represent a co-crystallized primitive macrocryst assemblage. Unfortunately, no clinopyroxene-hosted melt inclusions were observed, and thus a different approach is required to assess the degree of trace element equilibrium between clinopyroxene macrocrysts and other magmatic components.

Calculating equilibrium melt compositions from clinopyroxene macrocrysts

By using appropriate partition coefficients, equilibrium trace element contents of the melts from which the clinopyroxene macrocrysts have crystallized may be reconstructed from the trace element content of the crystals (Wade *et al.*, 2008; Winpenny & Maclennan, 2011). Partition coefficients are controlled by the crystal composition and the melt composition, as well as by the pressure and temperature of crystallization (e.g. Wood & Blundy, 1997). Sector zoning (Nakamura, 1973) and crystal growth rates (Lofgren *et al.*, 2006) also affect partition coefficients in clinopyroxene, which are thus subject to large uncertainties. Errors in partition coefficients subsequently propagate into errors in equilibrium melt compositions calculated from clinopyroxene compositions.

Following the methods of Winpenny & Maclennan (2011), the degree of equilibrium between clinopyroxene macrocrysts, melt inclusions and matrix glass was assessed using Ce/Yb. Reasons for using Ce/Yb are two-fold: first, Ce and Yb are the light rare earth element (LREE) and heavy rare earth element (HREE) measured with the highest precision in clinopyroxene (1σ relative errors of 9% and 8%, respectively); second, the partitioning behaviour of both elements can be related through the lattice strain model (LSM) (Wood & Blundy, 1997). The effects of crystal and melt compositions on partition coefficients are incorporated into the D_0 term of the Brice equation (Brice, 1975) used in the LSM, and therefore cancel out when calculating $Ce/Yb_{eqm\text{-}melt}$ from $Ce_{eqm\text{-}melt}$ and $Yb_{eqm\text{-}melt}$. Uncertainties in D_0 thus also cancel out. Errors associated with the pressure and temperature of crystallization nevertheless remain in the E_{M2} and RT terms of the LSM, but have only minor effects on D_{LREE}/D_{HREE} (Winpenny & Maclennan, 2011).

Partition coefficients were calculated at 1190°C and 0·5 kbar. An approximate pressure error of ± 0·25 kbar (1σ) corresponds to the precision of CO_2 analyses and to uncertainties in CO_2 solubility models (Neave *et al.*, 2014). The error in thermometry is ±45°C (1σ) (Putirka, 2008). Increasing the temperature from 1150 to 1230°C at 0·5 kbar increases D_{Ce}/D_{Yb} from 0·183 to 0·218 and results in a change of $Ce/Yb_{eqm\text{-}melt}$ from 6·57 to 7·73. Varying the pressure from 0·001 to 1·5 kbar has a negligible effect on both absolute and relative partition coefficients. Furthermore, although increasing cooling rates increases the values of partition coefficients, it does not lead to significant changes in D_{LREE}/D_{HREE} (Lofgren *et al.*, 2006).

The mean $Ce/Yb_{eqm\text{-}melt}$ calculated from a total of 32 clinopyroxene macrocrysts is 7·20 and lies within the precision of LA-ICP-MS matrix glass analyses [Ce/Yb = 7·01 ±0·49 (1σ)]. A slightly larger difference is observed between $Ce/Yb_{eqm\text{-}melt}$ and matrix glass Ce/Yb measured by SIMS [6·55 ± 0·27 (1σ)], which is likely to result from different elemental fractionation effects and correction procedures between the two techniques. Good correspondence between matrix glass Ce/Yb and $Ce/Yb_{eqm\text{-}melt}$ calculated from clinopyroxene macrocrysts strongly suggests that clinopyroxene grew from a suite of melts closely related to the matrix glass.

Olivine-hosted melt inclusions have a mean Ce/Yb of 4·65 ± 0·85 (1σ) (Neave *et al.*, 2014) and plagioclase-hosted melt inclusions have a mean Ce/Yb of 5·28 ± 1·07 (1σ). The offset in Ce/Yb between olivine-hosted melt inclusions and plagioclase-hosted melt inclusions is comparable with the offset between Ce/Yb in matrix glasses measured by SIMS and LA-ICP-MS and is unlikely to be geologically significant. Cumulative probability distributions of Ce/Yb in melt inclusions and $Ce/Yb_{eqm\text{-}melt}$ from clinopyroxene macrocrysts are plotted in Fig. 15. Clinopyroxene macrocrysts are in equilibrium with significantly more incompatible trace element enriched compositions than either olivine-hosted or plagioclase-hosted melt inclusions. The Kolmogorov–Smirnov (KS) test was used to confirm whether plagioclase-hosted melt inclusions and clinopyroxene equilibrium melts are likely to be sourced from the same underlying composition distribution. The large value of the KS statistic ($D = 0{\cdot}822$) and the small p-value ($p = 2{\cdot}47 \times 10^{-8}$) indicate that it is extremely unlikely that plagioclase-hosted melt inclusions and clinopyroxene macrocrysts were sourced from the same population of melts.

Crystal accumulation recorded in crystal size distributions

Kinks in plagioclase CSDs can be accounted for by the accumulation of large plagioclase macrocrysts. All three samples for which CSDs were calculated have similar CSDs for small, high aspect ratio macrocrysts. However,

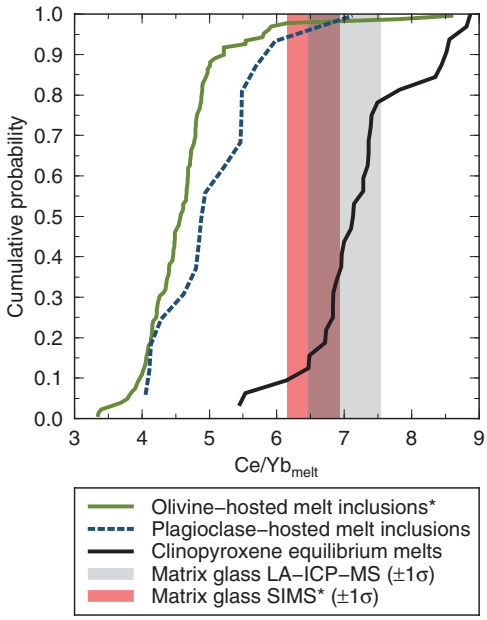

Fig. 15. Cumulative probability distributions of Ce/Yb in olivine-hosted melt inclusions from Neave *et al.* (2014), Ce/Yb in plagioclase-hosted melt inclusions and Ce/Yb of melts in equilibrium with clinopyroxene macrocrysts. Shaded regions show the composition of the matrix glass determined by LA-ICP-MS and SIMS (Neave *et al.*, 2014). Data from Neave et al. (2014) are marked with * in the legend. The difference in the probability distributions of olivine-hosted and plagioclase-hosted melt inclusions may be accounted for by a minor offset between LA-ICP-MS and SIMS analyses, which is also reflected in the composition of matrix glasses. Both suites of melt inclusions have much more depleted compositions than the matrix glass. The Ce/Yb values of melts predicted to be in equilibrium with clinopyroxene macrocrysts are similar to those of the matrix glass, and consequently they are more enriched than the melt inclusions. The details of the method used to determine the Ce/Yb of melts in equilibrium with clinopyroxene macrocrysts is discussed in the text.

the CSDs of large, low aspect ratio macrocrysts vary between samples. HOR-11-01B has the highest macrocryst content of the three samples (40·0%) and the highest population density of large plagioclase macrocrysts. Conversely, SKU-11-01B, which has the lowest macrocryst content (18·1%), also has the lowest population density of large plagioclase macrocrysts. Plagioclase CSDs are thus consistent with whole-rock geochemical variability being controlled by the accumulation of a plagioclase-rich assemblage. Considering plagioclase CSDs alongside QEMSCAN® images demonstrates that the accumulated population of large, low aspect ratio plagioclase crystals is composed of high-anorthite macrocrysts from the primitive assemblage. Whole-rock geochemistry and point counting systematics indicate, however, that plagioclase accumulates alongside olivine in the ratio ~9:1. The kink in the olivine CSD from HOR-11-01B may thus be explained by the accumulation of olivine alongside plagioclase. That other olivine CSDs are not kinked probably results from under-sampling of large olivine macrocrysts.

Small plagioclase macrocrysts, small olivine macrocrysts and clinopyroxene macrocrysts from the evolved population have straight CSDs. The population densities of evolved macrocrysts are thus probably controlled by crystal nucleation and growth (Cashman & Marsh, 1988); the evolved assemblage was not affected by either crystal accumulation or crystal settling.

Summary of macrocryst relationships

The two-stage crystallization history proposed on the basis of whole-rock geochemistry and point counting systematics in the previous section is well supported by microanalytical and textural observations. A primitive assemblage was generated in the first stage by crystallization of high-forsterite olivine and high-anorthite plagioclase, with minor chromite, from melts with an incompatible trace element depleted mean composition of Ce/Y ~ 0·47–0·48. An evolved assemblage was generated in the second stage by crystallization of low-forsterite olivine, low-anorthite plagioclase and clinopyroxene from melts with an incompatible trace element enriched mean composition of Ce/Y ~ 0·65–0·71, following variable accumulation of the primitive assemblage. Macrocrysts from the primitive assemblage occur in non-cotectic proportions—plg:ol in the ratio ~9:1 rather than in the ~7:3 ratio expected from cotectic crystallization (Grove *et al.*, 1992). Macrocrysts from the evolved assemblage are present in three-phase eutectic proportions. The erupted magma hence carries a full record of the second stage of crystallization, but a biased record of the first. In order to understand the origins of this biased record of crystallization it is necessary to consider how geochemically distinct macrocryst assemblages became juxtaposed. To constrain the role that magma reservoir dynamics may have played in determining macrocryst abundances and proportions of macrocrysts, the physical properties of both melts and macrocrysts must first be constrained.

Physical properties of melts and macrocrysts

Melt densities were calculated using the method of Bottinga & Weill (1970), with updated partial molar volumes and thermal expansion coefficients (Lange & Carmichael, 1990; Toplis *et al.*, 1994; Lange, 1997; Ochs & Lange, 1999). The effect of melt compressibility was accounted for by using compressibility coefficients from Lange & Carmichael (1990) and Ochs & Lange (1999). The pre-eruptive melt density was calculated using the average matrix glass composition and an H_2O content of 0·38 wt % (Neave *et al.*, 2014). Pressure and temperature were set at 0·5 kbar and 1190°C (see earlier sections). The densities of melts from which the primitive assemblage may have crystallized were estimated in two ways: first, density calculations were performed on the compositions of plagioclase-hosted melt inclusions; second, density

calculations were performed on melts in equilibrium with the primitive assemblage ($Mg\# = 64 \pm 2$ and $Ca/Na = 3{\cdot}8 \pm 0{\cdot}2$), selected from a large database ($n = 3480$) of Icelandic melt compositions [see Appendix 1 of Shorttle & Maclennan (2011), with further additions from Korneef *et al.* (2012)]. An H_2O content of 0·15–0·2 wt % was estimated for plagioclase-hosted melt inclusions and primitive melts from their TiO_2 content using the H_2O/TiO_2 of matrix glasses. Primitive melt densities were calculated at 0·5 kbar and 1230°C. The temperature of 1230°C was calculated using melt thermometry equations from Putirka (2008), and is consistent with liquidus temperatures calculated using the olivine–melt equilibria for appropriate forsterite contents (Ford *et al.*, 1983; Herzberg & O'Hara, 2002). Melt viscosities were calculated using he results of Giordano *et al.* (2008) for the same suite of melts and conditions. Melt densities and viscosities are given in Table 4.

Olivine and clinopyroxene densities were calculated at 1190°C and 1230°C using end-member densities and thermal expansion coefficients from Fei (1995) and Smyth & McCormick (1995). Plagioclase densities were calculated at An_{78} and An_{89} using molar volumes determined for these specific compositions by Angel *et al.* (1990). Thermal expansion coefficients were calculated using the parameterizations of Berman (1988) and Holland & Powell (1998) as presented by Tribaudino *et al.* (2010). Densities calculated using the Holland & Powell (1998) parameterization are $\sim 50\ kg\ m^{-3}$ lower than densities calculated using the Berman (1988) parameterization at the anorthite contents and temperatures considered. Although the Holland & Powell (1998) model accounts for the saturation of thermal expansion at high temperatures, the Berman (1988) model appears to provide a better fit at high temperatures (Tribaudino *et al.*, 2010). However, given that the Berman (1988) and Holland & Powell (1998) parameterizations are calibrated for lower temperature conditions than relevant for the Skuggafjöll magma, it is unclear which model should be favoured. Macrocryst densities, including plagioclase densities calculated with both the Berman (1988) and Holland & Powell (1998) models, are given in Table 4. An_{78} plagioclase, which is representative of low-anorthite plagioclase from the evolved macrocryst assemblage, is estimated to be $31–84\ kg\ m^{-3}$ less dense than the evolved melt immediately before eruption (Table 4). An_{89} plagioclase, which is representative of high-anorthite plagioclase from the primitive macrocryst assemblage, is estimated to be $8–62\ kg\ m^{-3}$ less dense than the primitive melts.

The density of melts is strongly dependent on their H_2O content (Ochs & Lange, 1999). Calculated melt densities are thus maxima because the assumption that subglacially quenched matrix glasses are H_2O-undersaturated may be invalid. Indeed, primitive melts in Iceland may contain up to 0·3 wt % H_2O (Nichols *et al.*, 2002) rather than the 0·15–0·2 wt % estimated here from H_2O/TiO_2. Increasing the H_2O content of primitive melts to 0·3 wt % decreases densities to $2689–2692\ kg\ m^{-3}$. Incorporating the effects of other volatiles, such as CO_2 and S, could reduce melt density further, increasing the likelihood of plagioclase flotation. Uncertainties in the density and hence buoyancy of high-anorthite plagioclase are unlikely to be resolvable until the thermal expansion behaviour of plagioclase is better constrained at magmatic temperatures. What is probable, however, is that plagioclase is close to neutral buoyancy and will thus have a much longer residence time in the magma reservoir than olivine.

Although density calculations are equivocal on the subject of plagioclase buoyancy, they imply that a troctolitic assemblage of plagioclase and olivine would be denser than the primitive melts: an assemblage containing 90% An_{89} plagioclase and 10% Fo_{86} olivine has a density of $2702–2748\ kg\ m^{-3}$ at 1230°C, which is $2–55\ kg\ m^{-3}$ higher than the density calculated for the primitive melts. Therefore, if plagioclase formed glomerocrysts with olivine, whether by synneusis (e.g. Schwindinger, 1999) or by heterogeneous nucleation (e.g. Kirkpatrick, 1981), then they would sink.

Requirements of an internally consistent petrogenetic model for Skuggafjöll

Diverse petrographic, geochemical and microanalytical observations place constraints on the fluid dynamic processes that took place during the assembly of the Skuggafjöll magma. Key observations that must be accounted for in any internally consistent petrogenetic model for Skuggafjöll are as follows. First, macrocrysts in the Skuggafjöll magma can be divided into two discrete assemblages, a primitive two-phase troctolitic assemblage and an evolved three-phase gabbroic assemblage. These two assemblages are separated by a compositional gap equivalent to a step in the degree of melt evolution from $Mg\# \sim 64$ to $Mg\# \sim 57$. Second, the primitive assemblage crystallized from melts with an incompatible trace element depleted mean composition ($Ce/Y \sim 0{\cdot}47–0{\cdot}48$), whereas the evolved assemblage crystallized from more incompatible trace element enriched melts ($Ce/Y \sim 0{\cdot}65–0{\cdot}71$) and is in trace element equilibrium with the matrix glass. Third, whole-rock geochemical variability results from variable accumulation of a primitive, troctolitic assemblage. All samples have crystallized similar amounts of the evolved gabbro assemblage. Fourthly, macrocrysts from the evolved assemblage are present in three-phase eutectic proportions, but macrocrysts from the primitive assemblage occur in somewhat variable, but strongly non-cotectic, proportions ($plg:ol \sim 9:1$). Finally, both the textural association of primocrystic high-anorthite plagioclase and high-forsterite olivine and the composition of melt inclusions hosted within these two phases require that both primitive plagioclase and olivine were, at least in part, accumulated concurrently.

Table 4: Predicted physical properties of melt and macrocrysts in the Skuggafjöll magma

Material	Melt H_2O (wt %)	Temperature (°C)	Plagioclase thermal expansion model	ρ (kg m^{-3})	μ (Pa s)
Melts					
Matrix glass	0·38	1190		2704	27
Primitive melts (MI)	~0·22	1230		2700	12
Primitive melts (eqm.)	~0·16	1230		2697	8
Primitive melts (MI)	0·30	1230		2692	12
Primitive melts (eqm.)	0·30	1230		2689	8
Macrocrysts					
Olivine Fo_{79}	–	1190		3365	–
Olivine Fo_{86}	–	1190		3285	–
Clinopyroxene Mg# 82	–	1190		3224	–
Plagioclase An_{78}	–	1190	HP	2620	–
Plagioclase An_{78}	–	1190	B	2673	–
Plagioclase An_{89}	–	1190	HP	2641	–
Plagioclase An_{89}	–	1190	B	2692	–
Olivine Fo_{79}	–	1230		3361	–
Olivine Fo_{86}	–	1230		3282	–
Clinopyroxene Mg# 82	–	1230		3221	–
Plagioclase An_{78}	–	1230	HP	2617	–
Plagioclase An_{78}	–	1230	B	2671	–
Plagioclase An_{89}	–	1230	HP	2638	–
Plagioclase An_{89}	–	1230	B	2689	–

MI, primitive melt compositions estimated from plagioclase-hosted melt inclusions; eqm., primitive melt compositions estimated from Icelandic melts in equilibrium with the primitive melt (see text for details); HP, plagioclase thermal expansion calculated using the parameterization of Holland & Powell (1998); B, plagioclase thermal expansion calculated using the parameterization of Berman (1988).

The origin of non-cotectic proportions in the primitive macrocryst assemblage

During cooling of MORB-like compositions along the low-pressure two-phase cotectic, plagioclase and olivine are expected to crystallize in the ratio ~7:3 (e.g. Grove *et al.*, 1992). Given that primitive melt compositions inferred for Skuggafjöll are neither especially calcic nor aluminous (see Panjasawatwong *et al.*, 1995), the cotectic proportions determined by Grove *et al.* (1992) for MORB crystallization are expected to be valid for Skuggafjöll. The plg:ol ~ 9:1 ratio observed in the primitive assemblage is, however, significantly enriched in plagioclase with respect to cotectic proportions. Lange *et al.* (2013*a*) suggested that similarly high plg:ol ratios in PUBs can be explained either by entrainment of non-cotectic cumulates, by separation of dense olivine from lighter plagioclase during ascent through the crust, or by some combination of these two processes. That the evolved assemblage occurs in three-phase eutectic proportions rules out the possibility of significant macrocryst fractionation during final ascent at Skuggafjöll: if the primitive assemblage was enriched in plagioclase or depleted in olivine at this stage, then similar changes in phase proportions would be expected in the evolved assemblage. Entrainment of primitive macrocrysts from non-cotectic cumulates is, however, an appealing mechanism by which plagioclase enrichment can be achieved. In particular, macrocryst entrainment is capable of explaining the presence of distinct macrocryst assemblages separated in their degree of incompatible trace element enrichment as well as in their degree of evolution. Before discussing the implications of macrocryst entrainment for highly phyric basalt genesis at Skuggafjöll and elsewhere, it is important to consider whether accumulation of crystals by cumulate disaggregation is consistent with the observations presented in preceding sections.

Crystal or mush entrainment?

Geochemical and petrographic arguments have been used to argue that crystals have accumulated in magmas in a range of systems by entrainment of crystals alone

(e.g. Salaün *et al.*, 2010) or mushes (i.e. crystals + melt) (e.g. Holness *et al.*, 2007; Costa *et al.*, 2010; Passmore *et al.*, 2012). Regressions of whole-rock compositions against point counting data from Skuggafjöll predict incompatible element concentrations close to zero at macrocryst mass fractions of unity (Fig. 14a; Supplementary Data Electronic Appendix 8). At first inspection, such regressions appear to suggest that macrocrysts were added from a solid cumulate without any interstitial mush liquid in equilibrium with the primitive macrocrysts. However, entraining crystals from a loosely packed mush is more probable than entraining crystals from a solid cumulate of intergrown crystals. Furthermore, rock microstructures visible optically and on QEMSCAN® images indicate that the primitive macrocrysts were stored in a crystal mush and that this mush contained an appreciable volume of interstitial liquid (e.g. Fig. 2b and 'C' in Fig. 10). This apparent conflict between petrographic observations and whole-rock geochemistry must be accounted for.

Accumulated primitive macrocrysts as mush crystals

High-anorthite plagioclase macrocrysts in large glomerocrysts often rest at high angles to each other (Fig. 2b), a texture that is characteristic of high-porosity, plagioclase-dominated mushes at early stages of formation (Holness, 2005; Holness *et al.*, 2012). Joining crystals by synneusis—an alternative mechanism for associating crystals—requires that crystals become oriented in positions of low interfacial energy whilst free in the magma reservoir (Vance, 1969; Schwindinger, 1999), a situation that becomes increasingly unlikely as more crystals become joined (Dowty, 1980; Welsch *et al.*, 2013). Given that most large glomerocrysts contain seemingly randomly oriented grains, synneusis is not a viable explanation for the formation of all large glomerocrysts at Skuggafjöll.

Although simple models of cumulate and mush formation by crystal settling, as implied by Wager *et al.* (1960), have come under subsequent scrutiny (e.g. Campbell, 1978), both microanalytical and textural lines of evidence suggest that primitive macrocrysts at Skuggafjöll were processed via a dynamic magma reservoir, forming mushes by crystal settling or flotation rather than by *in situ* crystallization (Campbell, 1978). First, geochemical variability in primitive olivine-hosted melt inclusions is consistent with entrapment in a magma undergoing concurrent crystallization, mixing and CO_2 exsolution (Neave *et al.*, 2014). Second, crystals within single glomerocrysts often record different crystallization histories: some high-anorthite plagioclases contain no melt inclusions, whereas others contain concentric bands of small melt inclusions indicative of repeated minor resorption and crystallization events. Some high-anorthite cores show weak concentric zoning (~2 mol % An oscillations on ~5 μm lengthscales) that is probably related to subtle changes in melt chemistry (Ginibre *et al.*, 2002; Neave *et al.*, 2013). Other grains are unzoned, implying growth from melts with buffered compositions. It should be noted, however, that mush formation by crystal settling or flotation as described here does not rule out growth during earlier phases of *in situ* crystallization, after which crystals were entrained, shuffled by mixing and deposited (e.g. Tepley & Davidson, 2003).

Small and complex interstices between high-anorthite and high-forsterite macrocrysts were more likely to have been filled by a melt than by crystals prior to disaggregation and entrainment ('C' in Fig. 10). Additionally, the presence of planar crystal faces within glomerocrysts suggests that some mush crystal faces continued to grow unimpeded into open melt following impingement (Cabane *et al.*, 2005). Thin melt films between crystals and melt pores at plg–plg–plg grain boundaries that have solidified to mesostasis attest to the presence of an interstitial mush liquid between primitive mush crystals (Fig. 2d). The arrangement of primitive macrocrysts therefore suggests that an interstitial liquid was present before mush disaggregation.

The fate of the interstitial mush liquid

The method of identifying mush addition outlined by Passmore *et al.* (2012) for the Laki eruption holds true only if mush crystals and the mush liquid remain coupled during mixing into the carrier liquid. If the mush liquid and mush crystals become decoupled, then the proportion of mush crystals in a sample need not correlate with the proportion of mush liquid. Stirring a mush into its carrier liquid by vigorous convection could result in homogenization of carrier and mush liquids if compositional heterogeneities are sufficiently reduced in size to allow diffusive mixing (Maclennan, 2008; Costa *et al.*, 2010), but may also homogenize crystal contents. The inhomogeneity of crystal content across the Skuggafjöll eruption (accumulated macrocryst mass fractions span the range 0–35%) casts doubt on the ability of post-entrainment mixing to homogenize the melt composition. If mixing were sufficiently vigorous to mix evolved and primitive melts without leaving a record in macrocryst compositions, then homogenization of entrained crystals across the eruption might have been expected, macrocryst self-organization as a result of complex two-phase flow notwithstanding (e.g. Burgisser *et al.*, 2005).

Alternatively, if the original mush liquid was replaced by or re-equilibrated with the carrier liquid prior to disaggregation, then no record of the original, primitive mush liquid would remain, except in melt inclusions (Fig. 2d). Observations on plagioclase-rich nodules erupted from a series of tuff cones close to Skuggafjöll (Brandur, Fontur and Saxi) demonstrate the viability of mush liquid replacement or re-equilibration. Detailed geochemical and petrographic descriptions of the nodules have been provided by Hansen & Grönvold (2000) and Holness *et al.* (2007) respectively. Compositions and textures of macrocrysts within these nodules are indistinguishable from

those in primitive macrocrysts from Skuggafjöll. Crucially, the composition of glass within the nodules is very similar to the composition of their evolved carrier liquids (Hansen & Grönvold, 2000), and is far from being in equilibrium with the primitive nodule macrocrysts. By considering the relative rates of diffusion in matrix or nodule glasses and olivine macrocrysts, it is possible to assess whether a primitive mush liquid could re-equilibrate with a more evolved carrier liquid sufficiently quickly to leave minimal trace in the mush crystals.

Assuming neutral species diffusion, the Mg–Fe interdiffusion coefficient for Skuggafjöll matrix glasses is $4{\cdot}14 \times 10^{-11}$ m^2 s^{-1} at 1200°C (Darken, 1948; Zhang, 2010). Coefficients for Mg and Fe^{2+} self-diffusion at 1200°C were taken from the experiments of Kress & Ghiorso (1995). Given that diffusion occurred within a crystal mush rather than in an open melt, corrections were applied to account for the effects of crystal shape and porosity by multiplying the diffusion coefficient by $\pi/2$ and 0·4 respectively (Thomson & Maclennan, 2013). A porosity of 0·4 is consistent with that measured in olivine-rich mush layers (Jerram *et al.*, 1996), but is lower than the 0·6 porosity estimated for plagioclase-rich cumulates from the Skaergaard and Sept-Îles layered intrusions (Tegner *et al.*, 2009; Namur & Charlier, 2012). An interdiffusion coefficient of $2{\cdot}61 \times 10^{-11}$ m^2 s^{-1} thus represents the lower bound of likely diffusivities within the Skuggafjöll mush liquid. Using the relationship $\sqrt{(Dt)} = L/2$, melt re-equilibrates across 5 cm in 7·6 years. The 5 cm lengthscale is significant because it is the minimum distance over which re-equilibration must have occurred in 10 cm diameter nodules from Brandur, Fontur and Saxi (Hansen & Grönvold, 2000). Diffusive re-equilibration may have taken place at a range of scales during the evolution of the Skuggafjöll mush. Melt may have been introduced to the magma reservoir via metre-scale intrusions or by intergranular flow on the centimetre scale, thus altering diffusive timescales accordingly.

Over 7·6 years, the lengthscale of Mg–Fe interdiffusion within olivine macrocrysts is 88 μm using an Mg–Fe interdiffusion coefficient of $8{\cdot}08 \times 10^{-17}$ m^2 s^{-1} (Fo_{80} at 1200°C and 0·5 kbar; Dohmen & Chakraborty, 2007). An 88 μm lengthscale is comparable in size with the width of low-forsterite rims in high-forsterite macrocrysts on QEMSCAN® images (Fig. 10). NaSi–CaAl interdiffusion in plagioclase under the same conditions is several orders of magnitude slower [$\sim(1\text{–}10) \times 10^{-21}$ m^2 s^{-1} in An_{70-90} at 1200°C; Grove *et al.*, 1984], resulting in a short diffusion lengthscale of <1 μm. Although a detailed study of mush disaggregation timescales is beyond the scope of this study, these calculations indicate that it is possible to reset the composition of mush liquids over short timescales whilst having only a modest effect on mush crystals.

Entrainment of primitive macrocrysts from non-cotectic crystal mushes fits within the requirements of an internally consistent petrogenetic model for Skuggafjöll. Fractionation of macrocryst phases must, however, still occur during the initial formation of mushes. A full fluid dynamic treatment of mush formation is beyond the scope of this study, and may not be possible within the currently available experimental framework (Burgisser *et al.*, 2005). Nevertheless, simple fluid dynamic and geological considerations suggest that non-cotectic mushes are likely to be produced following cotectic crystallization in dynamic magma reservoirs.

Speculation on the formation of non-cotectic crystal mushes

The rate at which crystals settle out from magma is strongly controlled by their density, even in vigorously convecting, turbulent magma reservoirs (Martin & Noakes, 1989; Burgisser *et al.*, 2005). Dense olivine macrocrysts thus settle rapidly: the Stokes' settling velocity of a 2 mm grain of forsteritic olivine in primitive melts from Skuggafjöll is $1{\cdot}1 \times 10^{-3}$ m s^{-1}. In contrast, high-anorthite plagioclase is close to neutral buoyancy in primitive melts from Skuggafjöll (Table 4). Assuming that the densities presented in Table 4 are correct and that plagioclase is positively buoyant, it is possible that plagioclase may float to reservoir roofs. The Stokes' settling velocity for a 2 mm grain of anorthitic plagioclase is $-(1{\cdot}9\text{–}11) \times 10^{-4}$ m s^{-1}. However, troctolitic glomerocrysts containing even a very small proportion of olivine will settle to the base: the Stokes' settling velocity for a 2 mm glomerocryst containing 90% plagioclase and 10% olivine is $(3{\cdot}5\text{–}84) \times 10^{-6}$ m s^{-1}.

Non-cotectic mushes and cumulates are likely to form following the crystallization of phases with different densities (Martin & Nokes, 1989). The first layers of mush deposited in magma reservoirs during cotectic crystallization of olivine and plagioclase will be dominated by dense olivine macrocrysts, because, at any given crystal size, plagioclase has a much longer residence time in basaltic reservoirs than olivine (Martin & Nokes, 1989). As a consequence, the non-mush portion of magma reservoirs will become enriched in plagioclase over time. This may lead to the segregation of macrocrysts into olivine-rich and plagioclase-rich mush layers by a range of mechanisms. If plagioclase is negatively buoyant, then the mush pile on the reservoir floor will be mineralogically stratified from an olivine-rich base to a plagioclase-rich top. If plagioclase is positively buoyant, then plagioclase mushes may develop at the top of the reservoir. However, the textural association of plagioclase with primocrystic olivine at Skuggafjöll suggests that some floated plagioclase may have delaminated and fallen to the base of the reservoir (e.g. Tepley & Davidson, 2003). Delamination from the reservoir roof could result from *in situ* heterogeneous

crystallization of olivine that generated gravitationally unstable troctolite mushes. Another possibility is that the magma reservoir reached the critical threshold to form crystal networks, locking crystals into an immobile, but porous mush (e.g. Holness *et al.*, 2012). Speculations aside, that non-cotectic troctolites and anorthosites are commonly observed in oceanic crust sections (e.g. Elthon, 1987; Perk *et al.*, 2007), ophiolites (e.g. Pallister & Hopson, 1981; Nicolas & Boudier, 2011) and layered intrusions (e.g. Haskin & Salpas, 1992; Irvine *et al.*, 1998) confirms that non-cotectic mushes and cumulates are a common product of magma differentiation.

Excavation of mineralogically stratified mushes provides one explanation for the accumulation of non-cotectic assemblages in highly phyric basalts. Accumulated assemblages would achieve cotectic proportions only if mush disaggregation were fully efficient for all phases. However, the conditions that restrict mush disaggregation to plagioclase-rich horizons in the case of PUBs is unclear, although the density of mush crystals, the degree of compaction and the extent of interstitial crystallization are all likely to be important factors. Although the mush formation and disaggregation processes discussed here are consistent with observations made on the Skuggafjöll eruption, they are without fluid dynamic validation. Nevertheless, this discussion seeks to demonstrate the importance of non-cotectic mush formation and disaggregation in basaltic plumbing systems. Investigating the behaviour of variably dense macrocrysts in magma reservoirs represents an important next step in the study of crystal mush and highly phyric basalt genesis.

Assembling the Skuggafjöll magma

The first process recorded in the products of the Skuggafjöll eruption is crystallization of high-forsterite olivine and high-anorthite plagioclase from primitive melts with an incompatible trace element depleted mean composition (Fig. 16a and b). Melt inclusion data indicate that this first stage of crystallization took place in a suite of diverse mantle melts undergoing concurrent mixing and crystallization. Given the paucity of evidence for continued magmatic activity at Skuggafjöll (e.g. hydrothermal systems), it is probable that magmatic evolution took place within small, transient magma reservoirs. Melt inclusion entrapment pressures constrain the depth of mixing and crystallization to 0·5 kbar (Neave *et al.*, 2014).

Primitive and evolved macrocryst assemblages crystallized from melts that are geochemically distinct both in terms of their degree of evolution (Mg# ~ 64 versus Mg# ~ 57) and their degree of incompatible trace element enrichment (mean Ce/Y ~ 0·47–0·48 versus mean Ce/Y ~ 0·65–0·71). Following storage in mineralogically stratified mushes, primitive macrocrysts interacted with more evolved melts prior to eruption. These evolved, incompatible trace element enriched melts need not be related to the melts from which the primitive assemblage crystallized, and may have differentiated deeper in the crust. The composition of the melt present in the magma reservoir must have changed rapidly to cause a step change in the equilibrium composition of macrocryst phases (e.g. $An_{>83}$ to $An_{<79}$; Fig. 9). Although primitive macrocrysts may become associated with the evolved carrier liquid via a range of mechanisms, two plausible scenarios are outlined in Fig. 16.

One mechanism of juxtaposing primitive and evolved components in the Skuggafjöll magma involves recharge of a magma reservoir containing primitive mushes by a more evolved and incompatible trace element enriched melt from below (Fig. 16c and d). A rapid shift in melt composition could be achieved by the extraction of primitive melt prior to the injection of evolved melt, or by the rapid overprinting of volumetrically insignificant primitive melt by mixing. Given that the addition of an interstitial mush liquid is not recorded in whole-rock compositions, the mush liquid may have equilibrated with the evolved melt before disaggregation. The preservation of high-forsterite cores in ~1 mm olivines limits the primitive mush macrocryst residence time to ~30 years (Larsson & Karlsson, 1975; Thomson & Maclennan, 2013). The short timescale between recharge, disaggregation and eruption indicates that these processes are likely to be closely linked.

Alternatively, a highly phyric magma carrying primitive macrocrysts may have been injected into a shallower reservoir containing evolved melts (Fig. 16e and f). Efficient mixing would have been required to homogenize primitive and evolved melts, and to decouple primitive macrocrysts from primitive melts prior to the growth of the evolved assemblage. The volume of evolved melt involved in mixing could have been small if it had a low Mg#. Sufficiently evolved melts are known from the EVZ: matrix glasses from the Laki eruption are substantially more evolved (Mg# ~ 40; Thordarson *et al.*, 1996) than matrix glasses from Skuggafjöll (Mg# ~ 53).

Following mixing of primitive macrocrysts with evolved melts, a second stage of crystallization at the three-phase gabbro eutectic is required in both scenarios to generate low-anorthite plagioclase, low-forsterite olivine and clinopyroxene. All erupted lavas experienced similar amounts of crystallization during this second stage. No fractionation of phases of different density took place between mush disaggregation and eruption, implying that the non-cotectic plg:ol ratio in the primitive assemblage must have been fixed by the end of mush entrainment.

Implications for highly phyric basalt genesis

Highly phyric basalts throughout Iceland's neovolcanic zones share many petrological characteristics with Skuggafjöll (Hansen & Grönvold, 2000; Halldorsson *et al.*, 2008). For example, plagioclase macrocrysts show strongly

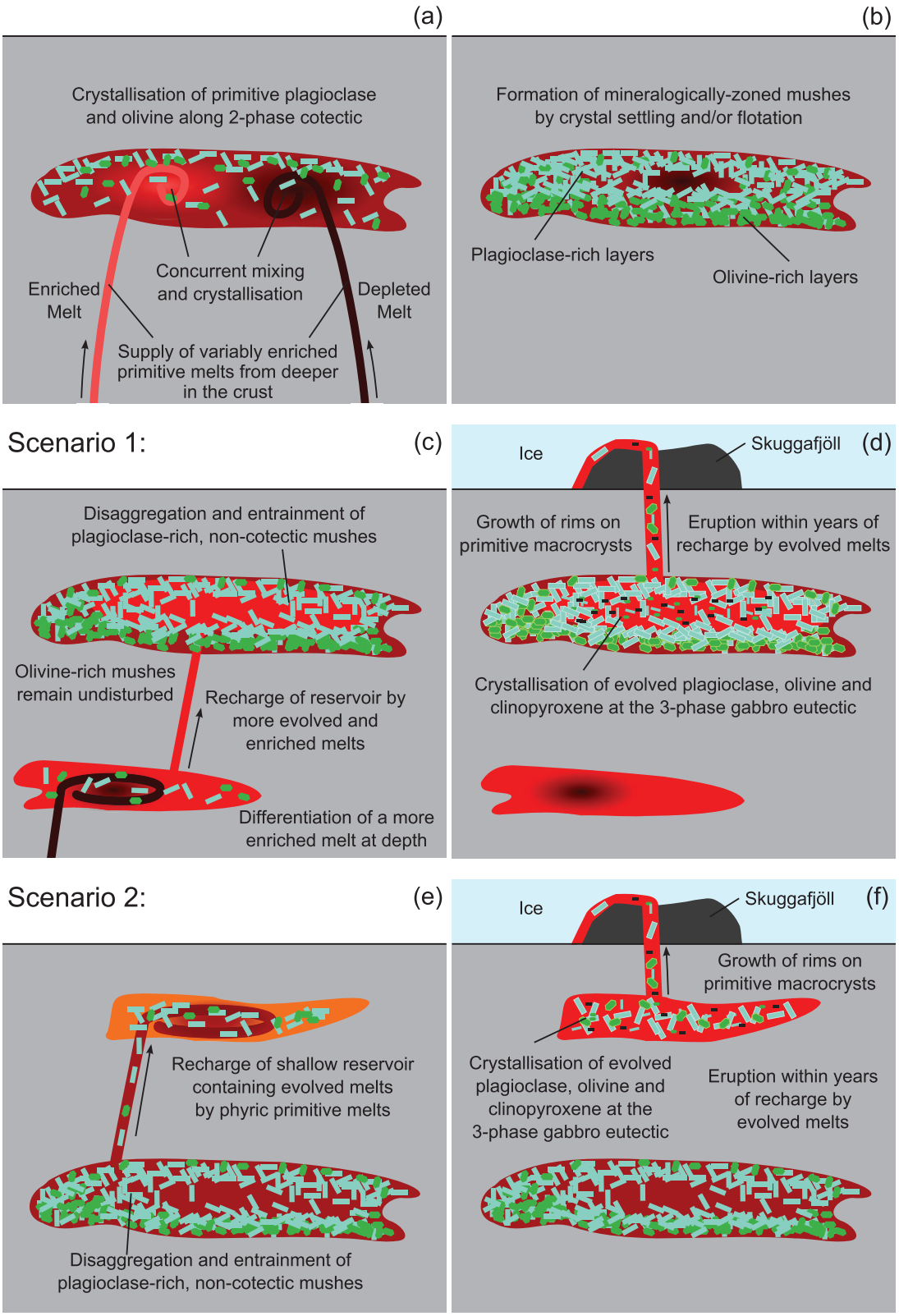

Fig. 16. Schematic illustration showing how the Skuggafjöll magma may have been assembled. (a) Primitive macrocrysts crystallize from geochemically variable melts in the shallow crust. Both olivine-hosted and plagioclase-hosted melt inclusions preserve a record of concurrent mixing and crystallization. (b) Crystal mushes develop on the margins of the magma reservoir and are likely to be mineralogically zoned. Association of primitive macrocrysts with evolved melts and macrocrysts can occur via range of mechanisms. Two possible scenarios are

(continued)

bimodal compositions, with high-anorthite cores (An_{80-90}) encased within low-anorthite (An_{60-80}) rims. Plagioclase macrocrysts dominate and form up to 30% of samples by volume (Hansen & Grönvold, 2000). The forsterite content of the volumetrically small amount of olivine (<5 vol. %) associated with high-anorthite plagioclase reaches ~Fo_{86}. Clinopyroxene occurs only in the most evolved samples and as an interstitial phase within primitive nodules carried by some highly phyric basalts (e.g. Holness *et al.*, 2007). Although insufficient phase proportion and whole-rock data are reported for other highly phyric basalts in Iceland to employ the techniques used in this study, macrocryst compositions and structures suggest that many eruptions across Iceland have experienced similar two-stage crystallization histories to Skuggafjöll. Up to 15–20% of the mass of highly phyric lavas in Iceland may thus be sourced from disaggregated mushes.

The entrainment of a troctolitic mush at Skuggafjöll implies that both olivine-rich and plagioclase-rich cumulates are present at depth in the EVZ crust. Transport of primitive melts to the shallow crust promotes early saturation of anorthitic plagioclase during fractional crystallization and the generation of plagioclase-rich troctolites (Panjasawatwong *et al.*, 1995; Kohut & Nielsen, 2003). The absence of $Fo_{>86}$ from eruptions in the EVZ (Hansen & Grönvold, 2000; Passmore, 2009; Moune *et al.*, 2012; Neave *et al.*, 2013) implies that the preceding olivine-only stage of crystallization is not recorded by erupted macrocrysts, possibly in part because of diffusive re-equilibration (Thomson & Maclennan, 2013). Diffusion aside, substantial amounts of dunitic material must thus reside at some depth within the EVZ crust to balance the mass of plagioclase-rich mushes and melts recorded at the surface: the most primitive melts erupted in the EVZ (Mg# ~ 64) are substantially more evolved than Icelandic primary melts (Mg# ~ 66–73; Shorttle & Maclennan, 2011), and thus experienced significant fractionation of olivine deeper in the crust. Such high-density dunitic cumulates may be resolvable with geophysical techniques (e.g. Kauahikaua *et al.*, 2000).

Primitive macrocrysts from Skuggafjöll, the Thjórsá lava and the Brandur, Fontur and Saxi tuff cones all preserve systematically more incompatible trace element depleted compositions than the melts in which they are erupted (this study; Halldorsson *et al.*, 2008). Trace element disequilibrium is supplemented by Sr isotopic disequilibrium in the cases of Thjórsá, Brandur, Fontur and Saxi (Halldorsson *et al.*, 2008). Although insufficient data are available to confirm whether or not this bias towards depletion in primitive macrocrysts is present across the EVZ, the observations available highlight the importance of evaluating the origin of magmatic components individually to constrain the diversity of mantle melt supply.

Early saturation of high-anorthite plagioclase in shallow magma reservoirs, crystal mush disaggregation and complex multi-stage crystallization histories are unlikely to be unique features of highly phyric basalt genesis in Iceland. High macrocryst contents and non-cotectic phase proportions in PUBs from mid-ocean ridge settings could also be generated by sequences of events similar to those inferred for Skuggafjöll (e.g. Lange *et al.*, 2013*a*). However, detailed investigations of intra-flow variability within submarine mid-ocean ridge lavas are rare because of sampling complexity (Rubin *et al.*, 2001; Soule *et al.*, 2012). Until large suites of samples have been collected from submarine PUBs, subaerial analogues such as Skuggafjöll provide a good route towards understanding the genesis of highly phyric basalts.

CONCLUSIONS

Strong correlations between major and trace element concentrations in whole-rock samples collected across the subglacial Skuggafjöll eruption in the EVZ of Iceland are controlled by macrocryst accumulation. Incompatible trace element ratios, such as Zr/Y, do not vary significantly between samples, indicating that mixing erased mantle-derived melt diversity by the time of eruption. Whole-rock element abundances correlate well with macrocryst mass fractions, which vary from 5·9 to 46·9%. Positive correlations between macrocryst content and whole-rock Sr and Ni concentrations confirm that plagioclase and olivine are responsible for controlling geochemical variability in whole-rock samples. Combined whole-rock and point counting systematics are best accounted for by accumulation of plagioclase and olivine in a strongly non-cotectic ratio (plg:ol ~ 9:1).

Phase proportions in the least phyric samples are similar to those expected from crystallization at the low-pressure three-phase gabbro eutectic (plg:cpx:ol ~ 11:6:3), whereas phase proportions in the most phyric samples are dominated by plagioclase (plg:cpx:ol ~ 8:1:1). Macrocrysts can be divided into two discrete assemblages using textural and compositional information in QEMSCAN® images: a

Fig. 16 Continued
outlined in (c) and (d), and (e) and (f), respectively. Scenario 1: (c) recharge of the primitive magma reservoir by more evolved melt triggers mush disaggregation; (d) crystallization of the evolved assemblage then occurs within the recharged reservoir immediately prior to eruption. Scenario 2: (e) a shallow, evolved magma reservoir experiences recharge by a phyric primitive melt; the macrocrysts in this phyric melt are derived by crystal mush disaggregation in a deeper reservoir; (f) following rapid and efficient mixing, crystallization of the evolved assemblage occurs.

primitive, troctolitic assemblage and an evolved gabbroic assemblage. The primitive assemblage consists of large, high-forsterite olivine and low aspect ratio, high-anorthite plagioclase macrocryst cores. The evolved assemblage consists of small, low-forsterite olivine, high aspect ratio, low-anorthite plagioclase and clinopyroxene macrocrysts, as well as rims around primitive macrocryst cores. This categorization of macrocrysts into assemblages is further supported by macrocryst trace element compositions and CSD.

Melt inclusions hosted within both high-forsterite olivine (Neave *et al.*, 2014) and high-anorthite plagioclase macrocrysts indicate that the primitive assemblage grew from incompatible trace element depleted melts (mean Ce/Y ~ 0·47–0·48). The compositions of matrix glasses and clinopyroxene macrocrysts indicate that the evolved assemblage grew from a suite of more incompatible trace element enriched parental melts (mean Ce/Y ~ 0·65–0·71) than the primitive assemblage. A two-stage crystallization model can account for changes in the degree of evolution and incompatible trace element enrichment between primitive and evolved assemblages. The first phase of crystallization (primitive assemblage) is separated from the second stage of crystallization (evolved assemblage) by the formation and partial disaggregation of crystal mushes. Entrainment from non-cotectic, mineralogically zoned mushes can explain non-cotectic proportions in the primitive macrocryst assemblage. Although there is no geochemical trace of an interstitial mush liquid in whole-rock samples, petrographic observations suggest that the primitive assemblage disaggregated from a high-porosity mush. Although detailed treatment of diffusion chronometry is beyond the scope of this study, simple calculations indicate that timescales between mush disaggregation and eruption are short—of the order of years. Magma recharge, mush disaggregation and eruption triggering processes are thus likely to be intimately related.

The identification of plagioclase-rich mush disaggregation in the Skuggafjöll magma implies that there are both olivine-rich and plagioclase-rich cumulates within the EVZ crust. Crystallization pressures of 0·5 kbar indicate that the EVZ upper crust is likely to contain large amounts of anorthitic plagioclase. On average, ~17% of the mass of the Skuggafjöll magma is composed of crystals that have been mobilized from storage in mushes and transported to the surface. Other highly phyric eruptions in Iceland and along the mid-ocean ridge system have similar macrocryst compositions, zonation patterns and phase proportions to the Skuggafjöll eruption. These striking petrological similarities suggest that the crystal content of highly phyric basalts, including PUBs, may be controlled by the disaggregation of non-cotectic crystal mushes.

ACKNOWLEDGEMENTS

Martin Walker and Robin Clark are thanked for their help with sample preparation at the University of Cambridge. Richard Walshaw helped with SEM imaging at the University of Leeds in the early phases of this study, and Giulio Lampronti helped with SEM imaging at the University of Cambridge. Nic Odling is thanked for preparing samples and performing XRF analyses at the University of Edinburgh. Iris Buisman and Jason Day assisted with EPMA and (LA-)ICP-MS analyses respectively at the University of Cambridge. Alan Butcher and Aukje Benedictus from FEI are thanked sincerely for performing QEMSCAN® analyses and processing the resulting data. We would also like to thank all the staff at the NERC Ion Microprobe Facility in Edinburgh, and Richard Hinton in particular, for facilitating SIMS analyses. Dan Morgan carried out high-resolution scanning of thin sections and has been the source of advice throughout. D.A.N. thanks Kathy Cashman and Marian Holness for incisive discussions that have greatly improved the robustness and clarity of this work, particularly with respect to textural analyses. Finally, we thank George Bergantz and Denis Geist for their encouraging reviews, and Marjorie Wilson for her editorial handling.

FUNDING

This work was supported by a Natural Environment Research Council Studentship to D.A.N. (NE/1528277/1). SIMS analyses were performed as part of a Natural Environment Research Council Ion Microprobe Project awarded to M.E.H. (IMF484/0513).

SUPPLEMENTARY DATA

Supplementary data for this paper are available at *Journal of Petrology* online.

REFERENCES

Adams, D. T., Nielsen, R. L., Kent, A. J. R. & Tepley, F. J., III (2011). Origin of minor and trace element compositional diversity in anorthitic feldspar phenocrysts and melt inclusions from the Juan de Fuca Ridge. *Geochemistry, Geophysics, Geosystems* **12**, Q12T11.

Albarède, F. (1996). High resolution geochemical stratigraphy of Mauna Kea flows from the Hawaii Scientific Drilling Project core. *Journal of Geophysical Research B: Solid Earth* **101**, 11841–11853.

Angel, R. J., Carpenter, M. A. & Finger, L. W. (1990). Structural variation associated with compositional variation and order–disorder behavior in anorthite-rich feldspars. *American Mineralogist* **7**, 150–162.

Bédard, J. H. (2005). Partitioning coefficients between olivine and silicate melts. *Lithos* **83**, 394–419.

Bédard, J. H. (2006). Trace element partitioning in plagioclase feldspar. *Geochimica et Cosmochimica Acta* **70**, 3717–3742.

Berman, R. G. (1988). Internally-consistent thermodynamic data for minerals in the system Na_2O–K_2O–CaO–MgO–FeO–Fe_2O_3–Al_2O_3–SiO_2–TiO_2–H_2O–CO_2. *Journal of Petrology* **29**, 445–522.

Bindeman, I. N. & Davis, A. M. (2000). Trace element partitioning between plagioclase and melt: investigation of dopant influence on partition behaviour. *Geochimica et Cosmochimica Acta* **64**, 2863–2878.

Blundy, J. D. & Wood, B. J. (1991). Crystal-chemical controls on the partitioning of Sr and Ba between plagioclase feldspar, silicate melts, and hydrothermal solutions. *Geochimica et Cosmochimica Acta* **55**, 193–209.

Bottinga, Y. & Weill, D. F. (1970). Densities of liquid silicate systems calculated from partial molar volumes of oxide components. *American Journal of Science* **269**, 169–182.

Breddam, K. (2002). Kistufell: Primitive melt from the Iceland mantle plume. *Journal of Petrology* **43**, 345–375.

Brice, J. C. (1975). Some thermodynamic aspects of the growth of strained crystals. *Journal of Crystal Growth* **28**, 249–253.

Bryan, W. B. (1983). Systematics of modal phenocryst assemblages in submarine basalts: Petrologic implications. *Contributions to Mineralogy and Petrology* **83**, 62–74.

Bryan, W. B. & Moore, J. G. (1977). Compositional variations of young basalts in the Mid-Atlantic Ridge rift valley near lat 36°49′N. *Geological Society of America Bulletin* **88**, 556–570.

Bryan, W. B., Thompson, G. & Ludden, J. N. (1981). Compositional variation in normal MORB from 22°–25°N: Mid-Atlantic Ridge and Kane Fracture Zone. *Journal of Geophysical Research B: Solid Earth* **86**, 11815–11836.

Burgisser, A., Bergantz, G. W. & Breidenthal, R. E. (2005). Addressing complexity in laboratory experiments: the scaling of dilute multiphase flows in magmatic systems. *Journal of Volcanology and Geothermal Research* **141**, 245–265.

Cabane, H., Laporte, D. & Provost, A. (2005). An experimental study of Ostwald ripening of olivine and plagioclase in silicate melts: implications for the growth and size of crystals in magmas. *Contributions to Mineralogy and Petrology* **150**, 37–53.

Campbell, I. H. (1978). Some problems with the cumulus theory. *Lithos* **11**, 311–323.

Cashman, K. V. & Marsh, B. D. (1988). Crystal size distribution (CSD) in rocks and the kinetics and dynamics of crystallization. 2. Makaopuhi lava lake. *Contributions to Mineralogy and Petrology* **99**, 277–291.

Costa, F., Coogan, L. & Chakraborty, S. (2010). The time scales of magma mixing and mingling involving primitive melts and melt–mush interaction at mid-ocean ridges. *Contributions to Mineralogy and Petrology* **159**, 371–387.

Cullen, A., Vicenzi, E. & McBirney, A. R. (1989). Plagioclase-ultraphyric basalts of the Galapagos archipelago. *Journal of Volcanology and Geothermal Research* **37**, 325–337.

Danyushevsky, L. V., McNeill, A. W. & Sobolev, A. V. (2002). Experimental and petrological studies of melt inclusions in phenocrysts from mantle-derived magmas: an overview of techniques, advantages and complications. *Chemical Geology* **183**, 5–24.

Darken, L. (1948). Diffusion, mobility and their interrelation through free energy in binary metallic systems. *Transactions of AIME* **175**, 184–201.

Davidson, J. P., Morgan, D. J., Charlier, B. L. A., Harlou, R. & Hora, J. M. (2007). Microsampling and isotopic analysis of igneous rocks: implications for the study of magmatic systems. *Annual Review of Earth and Planetary Sciences* **35**, 273–311.

Dohmen, R. & Chakraborty, S. (2007). Fe–Mg diffusion in olivine II: point defect chemistry, change of diffusion mechanisms and a model for calculation of diffusion coefficients in natural olivine. *Physics and Chemistry of Minerals* **34**, 409–430.

Dowty, E. (1980). Synneusis reconsidered. *Contributions to Mineralogy and Petrology* **74**, 75–84.

Dungan, M. A. & Rhodes, J. M. (1978). Residual glasses and melt inclusions in basalts from DSDP Legs 45 and 46: evidence for magma mixing. *Contributions to Mineralogy and Petrology* **431**, 417–431.

Eason, D. E. & Sinton, J. M. (2009). Lava shields and fissure eruptions of the Western Volcanic Zone, Iceland: Evidence for magma chambers and crustal interaction. *Journal of Volcanology and Geothermal Research* **186**, 331–348.

Elthon, D. (1987). Petrology of gabbroic rocks from the Mid-Cayman Rise Spreading Center. *Journal of Geophysical Research B: Solid Earth* **92**, 658–682.

Fei, Y. (1995). Thermal expansion. In: Ahrens, T. J. (ed.) *Mineral Physics and Crystallography: a Handbook of Physical Constants*. American Geophysical Union, pp. 29–44.

Fitton, J. G. & Godard, M. (2004). Origin and evolution of magmas on the Ontong Java Plateau. In: Fitton, G., Mahoney, J., Wallace, P. & Saunders, A. (eds) *Origin and Evolution of the Ontong Java Plateau. Geological Society, London, Special Publications* **229**, 151–178.

Fitton, J. G., Saunders, A. D., Larsen, L. M., Hardarson, B. S. & Norry, M. J. (1998). Volcanic rocks from the southeast Greenland margin at 63°N: composition, petrogenesis and mantle sources. *Procedings of the Ocean Drilling Program, Scientific Results* **152**, 331–350.

Flower, M. F. J. (1980). Accumulation of calcic plagioclase in ocean-ridge tholeiite: an indication of spreading rate? *Nature* **287**, 530–532.

Ford, C. E., Russell, D. G., Craven, J. A. & Fisk, M. R. (1983). Olivine–liquid equilibria: temperature, pressure and composition dependence of the crystal/liquid cation partition coefficients for Mg, Fe^{2+}, Ca and Mn. *Journal of Petrology* **24**, 256–265.

Ginibre, C., Wörner, G. & Kronz, A. (2002). Minor-and trace element zoning in plagioclase: implications for magma chamber processes at Parinacota volcano, northern Chile. *Contributions to Mineralogy and Petrology* **143**, 300–315.

Giordano, D., Russell, J. & Dingwell, D. (2008). Viscosity of magmatic liquids: A model. *Earth and Planetary Science Letters* **271**, 123–134.

Gottlieb, P., Wilkie, G., Sutherland, D., Suthers, S., Perera, K., Jenkins, B., Spencer, S., Butcher, A. & Rayner, J. (2000). Microscopy for process mineralogy applications. *JOM* **52**, 24–25.

Govindaraju, K., Potts, P. J., Webb, P. C. & Watson, J. S. (1994). 1994 report on Whin Sill dolerite WS-E from England and Pitscurrie Microgabbro PM-S from Scotland: Assessment by one hundred and four international laboratories. *Geostandards Newsletter* **18**, 211–300.

Grove, T. L., Baker, M. B. & Kinzler, R. J. (1984). Coupled CaAl–NaSi diffusion in plagioclase feldspar: Experiments and applications to cooling rate speedometry of many metamorphic environments. *Geochimica et Cosmochimica Acta* **48**, 2113–2121.

Grove, T. L., Kinzler, R. J. & Bryan, W. B. (1992). Fractionation of mid-ocean ridge basalt (MORB). In: Phipps-Morgan, J., Blackman, D. K. & Sinton, J. M. (eds) *Mantle Flow and Melt Generation at Mid-ocean Ridges*. American Geophysical Union **71**, 281–310.

Gurenko, A. A. & Chaussidon, M. (1995). Enriched and depleted primitive melts included in olivine from Icelandic tholeiites—Origin by melting of a single mantle column. *Geochimica et Cosmochimica Acta* **59**, 2905–2917.

Gurenko, A. A. & Sobolev, A. V. (2006). Crust–primitive magma interaction beneath neovolcanic rift zone of Iceland recorded in gabbro xenoliths from Midfell, SW Iceland. *Contributions to Mineralogy and Petrology* **151**, 495–520.

Halldorsson, S. A., Oskarsson, N., Gronvold, K., Sigurdsson, G., Sverrisdottir, G. & Steinthorsson, S. (2008). Isotopic-heterogeneity of the Thjorsa lava—Implications for mantle sources and crustal

processes within the Eastern Rift Zone, Iceland. *Chemical Geology* **255**, 305–316.

Hansen, H. & Grönvold, K. (2000). Plagioclase ultraphyric basalts in Iceland: the mush of the rift. *Journal of Volcanology and Geothermal Research* **98**, 1–32.

Haskin, L. A. & Salpas, P. A. (1992). Genesis of compositional characteristics of Stillwater AN-I and AN-II thick anorthosite units. *Geochimica et Cosmochimica Acta* **56**, 1187–1212.

Hellevang, B. & Pedersen, R. B. (2008). Magma ascent and crustal accretion at ultraslow-spreading ridges: constraints from plagioclase ultraphyric basalts from the Arctic mid-ocean ridge. *Journal of Petrology* **49**, 267–294.

Herzberg, C. & O'Hara, M. J. (2002). Plume-associated ultramafic magmas of Phanerozoic age. *Journal of Petrology* **43**, 1857–1883.

Higgins, M. D. (1996). Magma dynamics beneath Kameni volcano, Thera, Greece, as revealed by crystal size and shape measurements. *Journal of Volcanology and Geothermal Research* **70**, 37–48.

Higgins, M. D. & Chandrasekharam, D. (2007). Nature of Sub-volcanic Magma Chambers, Deccan Province, India: Evidence from Quantitative Textural Analysis of Plagioclase Megacrysts in the Giant Plagioclase Basalts. *Journal of Petrology* **48**, 885–900.

Hill, E., Blundy, J. D. & Wood, B. J. (2010). Clinopyroxene–melt trace element partitioning and the development of a predictive model for HFSE and Sc. *Contributions to Mineralogy and Petrology* **161**, 423–438.

Hinton, R. (1990). Ion microprobe trace element analysis of silicates: Measurement of multi-element glasses. *Chemical Geology* **83**, 11–25.

Holland, T. J. B. & Powell, R. (1998). An internally consistent thermodynamic data set for phases of petrological interest. *Journal of Metamorphic Geology* **16**, 309–343.

Holness, M. B. (2005). On the use of changes in dihedral angle to decode late-stage textural evolution in cumulates. *Journal of Petrology* **46**, 1565–1583.

Holness, M. B., Anderson, A. T., Martin, V. M., Maclennan, J., Passmore, E. & Schwindinger, K. (2007). Textures in partially solidified crystalline nodules: a window into the pore structure of slowly cooled mafic intrusions. *Journal of Petrology* **48**, 1243–1264.

Holness, M. B., Humphreys, M. C. S., Sides, R., Helz, R. T. & Tegner, C. (2012). Toward an understanding of disequilibrium dihedral angles in mafic rocks. *Journal of Geophysical Research* **117**, B06207.

Holness, M. B., Richardson, C. & Andersen, J. C. Ø. (2013). The Campsite Dykes: a window into the early post-solidification history of the Skaergaard Intrusion, East Greenland. *Lithos* **182–183**, 134–149.

Irvine, T. N., Andersen, J. C. Ø. & Brooks, C. K. (1998). Included blocks (and blocks within blocks) in the Skaergaard intrusion: Geologic relations and the origins of rhythmic modally graded layers. *Geological Society of America Bulletin* **110**, 1398–1447.

Irving, A. & Frey, F. (1984). Trace element abundances in megacrysts and their host basalts: constraints on partition coefficients and megacryst genesis. *Geochimica et Cosmochima Acta* **48**, 1201–1221.

Jakobsson, S. P. (1979). Petrology of recent basalts of the Eastern Volcanic Zone, Iceland. *Acta Naturalia Islandica* **26**, 1–103.

Jakobsson, S. P. & Gudmundsson, M. (2008). Subglacial and intraglacial volcanic formations in Iceland. *Jökull* 179–196.

Jerram, D. A., Cheadle, M. J., Hunter, R. H. & Elliott, M. T. (1996). The spatial distribution of grains and crystals in rocks. *Contributions to Mineralogy and Petrology* **125**, 60–74.

Jochum, K. P., Willbold, M., Raczek, I., Stoll, B. & Herwig, K. (2005). Chemical characterisation of the USGS reference glasses and BIR-1G Using EPMA, ID-TIMS, ID-ICP-MS and LA-ICP-MS. *Geostandards and Geoanalytical Research* **29**, 285–302.

Jochum, K. P., Weis, U., Stoll, B., Kuzmin, D., Yang, Q., Raczek, I., Jacob, D. E., Stracke, A., Birbaum, K., Frick, D. A., Günther, D. & Enzweiler, J. (2011). Determination of reference values for NIST SRM 610–617 glasses following ISO guidelines. *Geostandards and Geoanalytical Research* **35**, 397–429.

Kamenetsky, V. S., Eggins, S. M., Crawford, A. J., Green, D. H., Gasparon, M. & Falloon, T. J. (1998). Calcic melt inclusions in primitive olivine at 43°N MAR: evidence for melt–rock reaction/melting involving clinopyroxene-rich lithologies during MORB generation. *Earth and Planetary Science Letters* **160**, 115–132.

Kauahikaua, J., Hildenbrand, T. & Webring, M. (2000). Deep magmatic structures of Hawaiian volcanoes, imaged by three-dimensional gravity models. *Geology* **28**, 883–886.

Kirkpatrick, R. J. (1981). Kinetics of crystallization of igneous rocks. In: Lasaga, A. C. & Kirkpatrick, R. J. (eds) *Kinetics of Geochemical Processes. Mineralogical Society of America, Reviews in Mineralogy* **8**, 321–398.

Kohut, E. J. & Nielsen, R. L. (2003). Low-pressure phase equilibria of anhydrous anorthite-bearing mafic magmas. *Geochemistry, Geophysics, Geosystems* **10**, 420–435.

Koornneef, J. M., Stracke, A., Bourdon, B., Meier, M. A., Jochum, K. P., Stoll, B. & Grönvold, K. (2012). Melting of a two-component source beneath Iceland. *Journal of Petrology* **53**, 127–157.

Kress, V. & Ghiorso, M. (1995). Multicomponent diffusion in basaltic melts. *Geochimica et Cosmochima Acta* **59**, 313–324.

Lange, A. E., Nielsen, R. L., Tepley, F. J., III & Kent, A. J. R. (2013*a*). The petrogenesis of plagioclase-phyric basalts at mid-ocean ridges. *Geochemistry, Geophysics, Geosystems* **14**, 3282–3296.

Lange, A. E., Nielsen, R. L., Tepley, F. J., III & Kent, A. J. R. (2013*b*). Diverse Sr isotope signatures preserved in mid-oceanic-ridge basalt plagioclase. *Geology* **41**, 279–282.

Lange, R. A. (1997). A revised model for the density and thermal expansivity extension to crustal magmatic temperatures. *Contributions to Mineralogy and Petrology* **130**, 1–11.

Lange, R. A. & Carmichael, I. S. E. (1990). Thermodynamic properties of silicate liquids with emphasis on density, thermal expansion and compressibility. In: Nicholls, J. & Russell, J. K. (eds) *Modern Methods of Igneous Petrology: Understanding Magmatic Processes. Mineralogical Society of America, Reviews in Mineralogy* **24**, 25–64.

Larsson, L. & Karlsson, B. (1975). Homogenization by one-phase diffusion. *Material Sciences and Engineering* **20**, 155–160.

Lofgren, G. E., Huss, G. R. & Wasserburg, G. J. (2006). An experimental study of trace element partitioning between Ti–Al-clinopyroxene and melt: Equilibrium and kinetic effects including sector zoning. *American Mineralogist* **91**, 1596–1606.

Maclennan, J. (2008). Concurrent mixing and cooling of melts under Iceland. *Journal of Petrology* **49**, 1931–1953.

Maclennan, J., McKenzie, D., Grönvold, K. & Slater, L. (2001). Crustal accretion under northern Iceland. *Earth and Planetary Science Letters* **191**, 295–310.

Maclennan, J., McKenzie, D., Grönvold, K., Shimizu, N., Eiler, J. M. & Kitchen, N. (2003*a*). Melt mixing and crystallization under Theistareykir, northeast Iceland. *Geochemistry, Geophysics, Geosystems* **4**, 8624.

Maclennan, J., McKenzie, D., Hilton, F., Grönvold, K. & Shimizu, N. (2003*b*). Geochemical variability in a single flow from northern Iceland. *Journal of Geophysical Research* **108**, 1–21.

Marsh, B. D. (1988). Crystal size distribution (CSD) in rocks and the kinetics and dynamics of crystallization. 1. Theory. *Contributions to Mineralogy and Petrology* **99**, 277–291.

Marsh, B. D. (1998). On the interpretation of crystal size distributions in magmatic systems. *Journal of Petrology* **39**, 553–599.

Martin, D. & Nokes, R. (1989). A fluid-dynamical study of crystal settling in convecting magmas. *Journal of Petrology* **30**, 1471–1500.

Mathews, W. H., Thorarinsson, S. & Church, N. B. (1964). Gravitative settling of olivine in pillows of an Icelandic basalt. *American Journal of Science* **262**, 1036–1040.

McKenzie, D. & O'Nions, R. K. (1998). Melt production beneath oceanic islands. *Physics of the Earth and Planetary Interiors* **107**, 143–182.

Moune, S., Sigmarsson, O., Schiano, P., Thordarson, T. & Keiding, J. K. (2012). Melt inclusion constraints on the magma source of Eyjafjallajökull 2010 flank eruption. *Journal of Geophysical Research* **117**, 1–13.

Nakamura, Y. (1973). Origin of sector-zoning of igneous clinopyroxenes. *American Mineralogist* **58**, 986–990.

Namur, O., Charlier, B., Pirard, C., Hermann, J., Liégeois, J.-P. & Vander Auwera, J. (2011*a*). Anorthosite formation by plagioclase flotation in ferrobasalt and implications for the lunar crust. *Geochimica et Cosmochimca Acta* **75**, 4998–5018.

Namur, O., Charlier, B., Toplis, M. & Vander Auwera, J. (2011*b*). Prediction of plagioclase–melt equilibria in anhydrous silicate melts at 1-atm. *Contributions to Mineralogy and Petrology* **163**, 133–150.

Namur, O. & Charlier, B. (2012). Efficiency of compaction and compositional convection during mafic crystal mush solidification: the Sept Îles layered intrusion, Canada. *Contributions to Mineralogy and Petrology* **163**, 1049–1068.

Neave, D. A., Passmore, E., Maclennan, J., Fitton, G. & Thordarson, T. (2013). Crystal–melt relationships and the record of deep mixing and crystallization in the AD 1783 Laki eruption, Iceland. *Journal of Petrology* **54**, 1661–1690.

Neave, D. A., Maclennan, J., Edmonds, M. E. & Thordarson, T. (2014). Melt mixing causes anticorrelation of trace element enrichment and CO_2 content prior to an Icelandic eruption. *Earth and Planetary Science Letters* **400**, 272–283.

Nichols, A. R. L., Carroll, M. R. & Höskuldsson, Á. (2002). Is the Iceland hot spot also wet? Evidence from the water contents of undegassed submarine and subglacial pillow basalts. *Earth and Planetary Science Letters* **202**, 77–87.

Nicolas, A. & Boudier, F. (2011). Structure and dynamics of ridge axial melt lenses in the Oman ophiolite. *Journal of Geophysical Research* **116**, B03103.

Nielsen, R. L. (2011). The effects of re-homogenization on plagioclase hosted melt inclusions. *Geochemistry, Geophysics, Geosystems* **12**, Q0AC17.

Nielsen, R. L., Crum, J., Bourgeois, R., Hascall, K., Forsythe, L. M., Fisk, M. R. & Christie, D. M. (1995). Melt inclusions in high-An plagioclase from the Gorda Ridge: an example of the local diversity of MORB parent magmas. *Contributions to Mineralogy and Petrology* **122**, 34–50.

Ochs, F. A. & Lange, R. A. (1999). The density of hydrous magmatic liquids. *Science* **283**, 1314–1317.

Óskarsson, N., Helgason, Ö. & Steinthórsson, S. (1994). Oxidation state of iron in mantle-derived magmas of the Icelandic rift zone. *Hyperfine Interactions* **91**, 733–737.

Pallister, J. S. & Hopson, C. A. (1981). Samail ophiolite plutonic suite: field relations, phase variation, cryptic variation and layering, and a model of a spreading ridge magma chamber. *Journal of Geophysical Research* **86**, 2593–2644.

Panjasawatwong, Y., Danyushevsky, L. V., Crawford, A. J. & Harris, K. L. (1995). An experimental study of the effects of melt composition on plagioclase–melt equilibria at 5 and 10 kbar: implications for the origin of magmatic high-An plagioclase. *Contributions to Mineralogy and Petrology* **118**, 420–432.

Passmore, E. (2009). Feeding large eruptions: Crystallisation, mixing and degassing in Icelandic magma chambers, PhD thesis, University of Edinburgh.

Passmore, E., Maclennan, J., Fitton, G. & Thordarson, T. (2012). Mush disaggregation in basaltic magma chambers: evidence from the AD 1783 Laki eruption. *Journal of Petrology* **35**, 2593–2623.

Perk, N. W., Coogan, L. A., Karson, J. A., Klein, E. M. & Hanna, H. D. (2007). Petrology and geochemistry of primitive lower oceanic crust from Pito Deep: implications for the accretion of the lower crust at the Southern East Pacific Rise. *Contributions to Mineralogy and Petrology* **154**, 575–590.

Pirrie, D., Butcher, A. R., Power, M. R., Gottlieb, P. & Miller, G. L. (2004). Rapid quantitative mineral and phase analysis using automated scanning electron microscopy (QemSCAN); potential applications in forensic geoscience. In: Pye, K. & Croft, D. J. (eds) *Forensic Geoscience: Principles, Techniques and Applications. Geological Society, London, Special Publication* **232**, 123–136.

Putirka, K. D. (2008). Thermometers and barometers for volcanic systems. In: Putirka, K. D. & Tepley, F. J., III (eds) *Minerals, Inclusions and Volcanic Processes. Mineralogical Society of America and Geochemical Society, Reviews in Mineralogy and Geochemistry* **69**, 61–120.

Rhodes, J. M., Dungan, M. A., Blanchard, D. P. & Long, P. E. (1979). Magma mixing at mid-ocean ridges: evidence from basalts drilled near 22°N on the Mid-Atlantic Ridge. *Tectonophysics* **55**, 35–61.

Ridley, W. I., Perfit, M. R., Smith, M. C. & Fornari, D. J. (2006). Magmatic processes in developing oceanic crust revealed in a cumulate xenolith collected at the East Pacific Rise, 9°50'N. *Geochemistry, Geophysics, Geosystems* **7**, Q12O04.

Roeder, P. L. & Emslie, R. F. (1970). Olivine–liquid equilibrium. *Contributions to Mineralogy and Petrology* **29**, 275–289.

Rubin, K. H., Smith, M. C., Bergmanis, E. C., Perfit, M. R., Sinton, J. M. & Batiza, R. (2001). Geochemical heterogeneity within mid-ocean ridge lava flows: insights into eruption, emplacement and global variations in magma generation. *Earth and Planetary Science Letters* **188**, 349–367.

Rudge, J. F. (2008). Finding peaks in geochemical distributions: A re-examination of the helium-continental crust correlation. *Earth and Planetary Science Letters* **274**, 179–188.

Ruprecht, P., Bergantz, G. W., Cooper, K. M. & Hildreth, W. (2012). The crustal magma storage system of Volcan Quizapu, Chile, and the effects of magma mixing on magma diversity. *Journal of Petrology* **53**, 801–840.

Salaün, A., Villemant, B., Semet, M. P. & Staudacher, T. (2010). Cannibalism of olivine-rich cumulate xenoliths during the 1998 eruption of Piton de la Fournaise (La Réunion hotspot): Implications for the generation of magma diversity. *Journal of Volcanology and Geothermal Research* **198**, 187–204.

Schwindinger, K. (1999). Particle dynamics and aggregation of crystals in a magma chamber with application to Kilauea Iki olivines. *Journal of Volcanology and Geothermal Research* **88**, 209–238.

Shorttle, O. & Maclennan, J. (2011). Compositional trends of Icelandic basalts: Implications for short-lengthscale lithological heterogeneity in mantle plumes. *Geochemistry, Geophysics, Geosystems* **12**, Q11008.

Sigmarsson, O., Condomines, M., Gronvöld, K., Thordarson, T. & Grönvold, K. (1991). Extreme magma homogeneity in the 1783–84 Lakagigar eruption: origin of a large volume of evolved basalt in Iceland. *Geophysical Research Letters* **18**, 2229–2232.

Sinton, C., Christie, D. & Coombs, V. (1993). Near-primary melt inclusions in anorthite phenocrysts from the Galapagos Platform. *Earth and Planetary Science Letters* **119**, 527–537.

Smyth, J. R. & McCormick, T. C. (1995). Crystallographic data for minerals. In: Ahrens, T. J. (ed.) *Mineral Physics and Crystallography: A Handbook of Physical Constants*. American Geophysical Union, pp. 1–17.

Sobolev, A. V. & Shimizu, N. (1993). Ultra-depleted primary melt included in an olivine from the Mid-Atlantic Ridge. *Nature* **363**, 151–154.

Sobolev, A. V., Hofmann, A. W. & Nikogosian, I. K. (2000). Recycled oceanic crust observed in 'ghost plagioclase' within the source of Mauna Loa lavas. *Nature* **404**, 986–990.

Soule, S. A., Nakata, D. S., Fornari, D. J., Fundis, A. T., Perfit, M. R. & Kurz, M. D. (2012). CO_2 variability in mid-ocean ridge basalts from syn-emplacement degassing: Constraints on eruption dynamics. *Earth and Planetary Science Letters* **327–328**, 39–49.

Sours-Page, R., Nielsen, R. L. & Batiza, R. (2002). Melt inclusions as indicators of parental magma diversity on the northern East Pacific Rise. *Chemical Geology* **183**, 237–261.

Tegner, C., Thy, P. & Holness, M. (2009). Differentiation and compaction in the Skaergaard Intrusion. *Journal of Petrology* **50**, 813–840.

Tepley, F. J., III & Davidson, J. P. (2003). Mineral-scale Sr-isotope constraints on magma evolution and chamber dynamics in the Rum layered intrusion, Scotland. *Contributions to Mineralogy Petrology* **145**, 628–641.

Thomson, A. & Maclennan, J. (2013). The distribution of olivine compositions in Icelandic basalts and picrites. *Journal of Petrology* **54**, 745–768.

Thordarson, T. & Höskuldsson, Á. (2008). Postglacial volcanism in Iceland. *Jökull* **58**, 197–228.

Thordarson, T., Self, S., Óskarsson, N. & Hulsebosch, T. (1996). Sulfur, chlorine, and fluorine degassing and atmospheric loading by the 1783–1784 AD Laki (Skaftár Fires) eruption in Iceland. *Bulletin of Volcanology* **58**, 205–225.

Thordarson, T., Self, S., Miller, D., Larsen, G. & Vilmundardóttir, E. (2003). Sulphur release from flood lava eruptions in the Veidivötn, Grímsvötn and Katla volcanic systems, Iceland. In: Oppenheimer, C., Pyle, D. & Barclay, J. (eds) *Volcanic Degassing. Geological Society, London, Special Publication* **213**, 103–121.

Toplis, M. J., Dingwell, D. B. & Libourel, G. (1994). The effect of phosphorus on the iron redox ratio, viscosity, and density of an evolved ferro-basalt. *Contributions to Mineralogy and Petrology* **117**, 293–304.

Tribaudino, M., Angel, R. J., Cámara, F., Nestola, F., Pasqual, D. & Margiolaki, I. (2010). Thermal expansion of plagioclase feldspars. *Contributions to Mineralogy and Petrology* **160**, 899–908.

Vance, J. A. (1969). On synneusis. *Contributions to Mineralogy and Petrology* **29**, 7–29.

Wade, J. A., Plank, T., Hauri, E. H., Kelley, K. A., Roggensack, K. & Zimmer, M. (2008). Prediction of magmatic water contents via measurement of H_2O in clinopyroxene phenocrysts. *Geology* **36**, 799–802.

Wager, L. R., Brown, G. M. & Wadsworth, W. J. (1960). Types of igneous cumulates. *Journal of Petrology* **1**, 73–85.

Welsch, B., Faure, F., Famin, V., Baronnet, A. & Bachelery, P. (2013). Dendritic crystallization: a single process for all the textures of olivine in basalts? *Journal of Petrology* **54**, 539–574.

Winpenny, B. & Maclennan, J. (2011). A partial record of mixing of mantle melts preserved in Icelandic phenocrysts. *Journal of Petrology* **52**, 1791–1812.

Wood, B. J. & Blundy, J. D. (1997). A predictive model for rare earth element partitioning between clinopyroxene and anhydrous silicate melt. *Contributions to Mineralogy and Petrology* **129**, 166–181.

Workman, R. K. & Hart, S. R. (2005). Major and trace element composition of the depleted MORB mantle (DMM). *Earth and Planetary Science Letters* **231**, 53–72.

Wright, T. L. & Doherty, P. C. (1970). A linear programming and least squares computer method for petrologic mixing problems. *Geological Society of America Bulletin* **81**, 1995–2008.

Yang, H.-J., Kinzler, R. J. & Grove, T. L. (1996). Experiments and models of anhydrous, basaltic olivine–plagioclase–augite saturated melts from 0·001 to 10 kbar. *Contributions to Mineralogy and Petrology* **124**, 1–18.

York, D. (1969). Least-squares fitting of a straight line with correlated errors. *Earth and Planetary Science Letters* **5**, 320–324.

Zellmer, G. F., Rubin, K. H., Grönvold, K. & Jurado-Chichay, Z. (2008). On the recent bimodal magmatic processes and their rates in the Torfajökull–Veidivötn area, Iceland. *Earth and Planetary Science Letters* **269**, 388–398.

Zhang, Y. (2010). Diffusion in minerals and melts: theoretical background. In: Zhang, Y. & Cherniak, D. J. (eds) *Diffusion in Minerals and Melts. Mineralogical Society of America and Geochemical Society, Reviews in Mineralogy and Geochemistry* **72**, 5–59.